POLITECNICO DI TORINO
Repository ISTITUZIONALE

Vat 3D printing of GelMA-dopa/MOFs composites wound dressings for precise photodynamic/photothermal therapy

Original
Vat 3D printing of GelMA-dopa/MOFs composites wound dressings for precise photodynamic/photothermal therapy / Wang, Y., Wei, Q., Frascella, F., Gaglio, C.G., Pirri, C.F., Jia, X., Xiao, A., Roppolo, I.. - In: BIOMATERIALS ADVANCES. - ISSN 2772-9508. - 191:(2027), pp. 1-14. [10.1016/j.bioadv.2026.215255]

Availability:
This version is available at: 11583/3017525 since: 2026-11-04T16:15:36Z

Publisher:
Elsevier

Published
DOI:10.1016/j.bioadv.2026.215255

Terms of use:

This article is made available under terms and conditions as specified in the corresponding bibliographic description in the repository

Publisher copyright

(Article begins on next page)

13 November 2026

Biomaterials Advances 191 (2027) 215255

Contents lists available at ScienceDirect

Biomaterials Advances

journal homepage: www.journals.elsevier.com/materials-science-and-engineering-c

Vat 3D printing of GelMA-dopa/MOFs composites wound dressings for precise photodynamic/photothermal therapy

Yang Wang [a], Qufu Wei [b,*], Francesca Frascella [c], Cesare Gabriele Gaglio [c], Candido Fabrizio Pirri [c], Xiaoli Jia [d], Anguo Xiao [a], Ignazio Roppolo [c,*]

[a] School of Chemistry and Materials Engineering, Hunan University of Arts and Science, Changde, Hunan, 415000, China
[b] Key Laboratory of Eco-textiles, Ministry of Education, Jiangnan University, Wuxi, 214122, China
[c] Department of Applied Science and Technology, Politecnico di Torino, Torino, 10124, Italy
[d] Department of Emergency Medicine, Shanghai Fourth People's Hospital, School of Medicine, Tongji University, Shanghai, 200434, China

ARTICLE INFO

Keywords:
DLP 3D printing
Light-triggered hydrogel
Programmable architecture
Porphyrinic MOFs
Environment-adaptive

ABSTRACT

Herein, we report a light-triggered hydrogel dressing fabricated via high-resolution digital light processing (DLP) 3D printing that seamlessly integrates programmable architecture with precisely tailored phototherapeutic functions. Dopamine-modified gelatin methacryloyl serves as the photocurable matrix, while glycerol is introduced to tune curing kinetics and improve optical transparency. Porphyrinic metal-organic frameworks (MOFs) are embedded as photoactive fillers to integrate both photodynamic and photothermal antibacterial functions. A facile $FeCl_3$ post-treatment strategy introduces dynamic Fe^{3+}-catechol coordination bonds into the 3D-printed hydrogel network, which remarkably boosts singlet oxygen ($^1O_2$) yield by 2.6-fold through a photocatalytic oxygen cycling. The obtained hydrogel dressing achieves 99.99% inactivation of *Staphylococcus aureus* and *Escherichia coli* within 15 min of irradiation, along with favorable biocompatibility. In full-thickness wound healing assays, the hydrogel mitigates inflammation and accelerates tissue regeneration, reaching ~89% wound closure within 12 days. Moreover, the glycerol-water binary solvent system endows the hydrogel with excellent anti-freezing and water retention properties, enabling stable operation in both extreme cold and dry-heat environments. This digitally programmable platform enables patient-specific, conformal dressings with environment-adaptive functionality, offering a scalable solution for remote and resource-limited.

1. Introduction

Bacterial infection is a major impediment to wound healing, delaying tissue repair and complicating the management of chronic wounds [1]. In this context, light-based antimicrobial strategies, particularly photodynamic therapy (PDT) and photothermal therapy (PTT), have emerged as promising alternatives because they are minimally invasive and are generally less prone to driving antimicrobial resistance than conventional antibiotics [2,3]. PDT eliminates bacteria by activating photosensitizers to generate reactive oxygen species (ROS), which induce irreversible oxidative damage to essential cellular components [4]. In contrast, PTT relies on photothermal agents to convert light into localized heat, leading to bacterial death through protein denaturation and disruption of membrane integrity [5].

Currently, various photosensitive materials—including black phosphorus, metal-organic frameworks (MOFs), MoS_2, and aggregation-induced emission luminogens (AIEgens)—have shown strong PDT/PTT efficacy and considerable potential for infected-wound treatment [6–9]. However, conventional topical administration of these nanoagents faces two major limitations. Mechanical friction and wound exudates can rapidly remove surface-applied agents, diminishing local concentration and therapeutic efficacy, while systemic absorption from the wound site may lead to phototoxic side effects [10,11]. To address these issues, hydrogel-based PDT/PTT platforms have been developed to physically confine photosensitive agents within polymer networks, thereby improving local retention and minimizing off-target exposure [10,12]. Moreover, hydrogels with high water retention, extracellular matrix-mimicking 3D networks, and favorable biocompatibility create a near-physiological microenvironment at the wound site. Such a milieu facilitates cell migration, proliferation, and differentiation, ultimately promoting tissue remodeling and functional recovery [12,13].

Nevertheless, the growing clinical demand for treating complex

* Corresponding authors.
E-mail addresses: qfwei@jiangnan.edu.cn (Q. Wei), ignazio.roppolo@polito.it (I. Roppolo).

https://doi.org/10.1016/j.bioadv.2026.215255
Received 14 July 2026; Received in revised form 13 October 2026; Accepted 14 October 2026
Available online 16 October 2026
2772-9508/© 2026 The Authors. Published by Elsevier B.V. This is an open access article under the CC BY-NC-ND license (http://creativecommons.org/licenses/by-nc-nd/4.0/).

wounds poses substantial challenges for the personalized application of phototherapeutic hydrogel dressings. This challenge arises from the inherent heterogeneity in wound tissue geometry, stiffness, and anatomical location [14,15]. Conventional bulk hydrogels with homogeneous architectures often fail to conform to irregular or anatomically constrained wound sites. In contrast, injectable hydrogels, owing to their low modulus, can readily adapt to uneven wound surfaces. Drug-loaded injectable hydrogel platforms have shown promising therapeutic outcomes in diseases such as osteomyelitis, periodontitis, and tenosynovitis [16–18]. However, they often suffer from limited mechanical robustness and rapid degradation, compromising durability during prolonged use. Alternatively, three-dimensional (3D) wound geometries can be acquired using scanning devices and translated into defect-matched hydrogel dressings via computer-aided 3D printing. Owing to their tunable physicochemical properties and precise structural customizability, advanced 3D-printed hydrogels have demonstrated broad applicability in the repair of complex tissues, including cartilage, muscle, nerves, and blood vessels [19–22]. Notably, 3D printing also enables remote, on-demand fabrication, offering considerable promise for future space exploration missions, where medical supplies are constrained and resupply from Earth is impractical.

Digital light processing (DLP)-based additive manufacturing is a high-precision, high-throughput 3D printing technology [23,24]. It employs a projector to selectively photopolymerize resins in a layer-by-layer manner, thereby enabling the accurate fabrication of complex 3D structures [25]. Compared with other 3D printing modalities, DLP offers distinct advantages, higher printing resolution and dimensional fidelity, faster fabrication, and improved surface quality [25,26]. Accumulating evidence indicates that DLP provides an effective route to engineer hydrogels with intricate 3D architectures from both synthetic and naturally derived precursors. Photocurable biomaterial matrices such as gelatin methacryloyl (GelMA), methacrylated hyaluronic acid, and silk fibroin-based derivatives have been widely explored for tissue engineering, wound repair, and drug delivery [27]. More importantly, DLP printing facilitates the precise in situ integration of diverse therapeutic drugs and nanoparticles within these matrixes, enabling the development of multifunctional dressings with tailored biological effects for precise and on-demand therapies. However, few DLP-printable hydrogel systems have been reported to simultaneously achieve favorable printing fidelity, anti-freezing tolerance and enhanced phototherapeutic activity. Furthermore, current DLP-printed phototherapeutic hydrogels mostly rely on direct loading of photosensitive fillers, and post-printing coordination chemistry to amplify synergistic PDT/PTT performance remains largely unexplored.

Building on these advancements, we developed a DLP-based phototherapeutic hydrogel platform that synergistically integrates programmable 3D architecture with chemically augmented photodynamic and photothermal functions. Specifically, using dopamine-modified GelMA (GMD) chemistry, we introduced a glycerol co-solvent system to simultaneously improve DLP processability and optical transparency. A porphyrinic MOFs (PCN-224), which integrate the Zr_6 clusters and porphyrin based molecular units into 3D network, were selected as photoactive fillers due to their dual photosensitizing capability. Importantly, we established a post-printing $FeCl_3$ treatment to construct Fe^{3+}-catechol coordination within the printed hydrogel. This facile coordination chemistry amplifies photodynamic and photothermal activities by 2.6-fold and 1.4-fold compared to untreated controls, respectively. We systematically evaluated the platform's antimicrobial efficacy against clinically relevant pathogens (*S. aureus* and *E. coli*), biocompatibility, and therapeutic performance in infected wound models. Furthermore, the glycerol-water binary network was examined for environmental resilience, extending applicability to extreme cold and arid conditions. This work demonstrates how digital fabrication, coordination chemistry, and rational material design can converge to create adaptable, patient-specific wound care solutions.

2. Experimental

2.1. Materials

Gelatin (Type B, from bovine skin), glycerol and water-soluble diphenyl (2,4,6-trimethylbenzoyl)phosphine oxide (TPO-SDS) were bought from Merck, Italy. $ZrOCl_2{\cdot}8H_2O$ (99.9%), 5,10,15,20-tetrakis(4-carboxyphenyl)porphyrin (TCPP, 97%), methacrylic anhydride (MA, 94%), dopamine hydrochloride (98%), N-(3-dimethylaminopropyl)-N′-ethylcarbodiimide hydrochloride (EDC, 98.5%), N-hydroxysuccinimide (NHS, 99%), 4-morpholineethanesulfonic acid (MES, 99.5%), Iron(III) chloride (99%), and poly(ethylene glycol) diacrylate (PEGDA, Mn = 575, 99%) were purchased from Macklin Biochemical Technology, China. 9,10-anthracenediyl-bis (methylene) dimalonic acid (ABDA, 90%), phosphate buffered saline (PBS, pH = 7.2), and tetracycline hydrochloride (TH, 90%) were purchased from Shanghai Vita Chemical Reagent, China. Benzoic acid (99.5%) and other chemicals were obtained from Sinopharm Chemical Reagent, China. Fresh rabbit blood was purchased from Qingdao Antiserum Biotechnology Co., Ltd., China, and L929 cells were obtained from Procell Life Science and Technology Co., Ltd., China. All chemicals were used as received without any additional purification.

2.2. Synthesis of GelMA

Gelatin methacryloyl (GelMA) was synthesized following a previously reported method with slight modification [28]. Briefly, gelatin powder (10 g) was dissolved in 100 mL of PBS at 50 °C. Then, 2 mL of MA was added dropwise to the mixture, which was kept under magnetic stirring (500 rpm) for 5 h. After the reaction, 400 mL of PBS was added, and the solution was dialyzed in deionized water using dialysis membranes (MWCO = 8–14 kDa) for 7 days at 40 °C. Finally, the dialyzed solution was freeze-dried to yield GelMA with a degree of substitution of approximately 60%.

2.3. Synthesis of GMD

GelMA-dopamine (GMD) was synthesized using a previously reported method [29]. In detail, 1.5 g of synthesized GelMA was dissolved in 150 mL of degassed MES buffer (50 mM, pH = 4.5) at 37 °C. EDC (862.6 mg) and NHS (518 mg) were then added to the solution. After stirring for 20 min, 853.4 mg of dopamine hydrochloride, pre-dissolved in 4.5 mL of MES buffer (50 mM, pH = 3.3), was mixed with the mixture. The reaction was conducted at 37 °C in darkness with shaking at 100 rpm for 24 h. The obtained product was transferred to a dialysis membrane (MWCO = 8–14 kDa) and dialyzed in a 0.001 mol/L HCl solution for two days, followed by one day in deionized water. Finally, the product was lyophilized to yield GMD. The content of dopamine grafted onto the GMD polymer was determined based on a standard curve established from the absorbance of dopamine solutions [30].

2.4. Synthesis of zirconium-based porphyrinic MOFs

Zirconium-based porphyrin-MOFs were synthesized following a previously reported method [31]. In detail, 3 g of benzoic acid and 300 mg of $ZrOCl_2{\cdot}8H_2O$ were dissolved in 20 mL DMF under ultrasonication for 20 min. Subsequently, 100 mg of TCPP was added to the solution, followed by additional ultrasonication for 30 min. After that, the mixture was transferred to a Teflon-lined autoclave and heated at 120 °C for 24 h. After the reaction, the mixture was cooled to room temperature naturally and centrifuged at 8000 rpm for 30 min to collect the precipitate. The precipitate was washed sequentially with DMF (twice) and with ethanol (three times) to remove impurities. Finally, The MOFs (PCN-224) nanocrystals were obtained after drying in a vacuum oven at 60 °C for 12 h.

2.5. Preparation of 3D printable formulations

The preparation of GMD/MOFs- glycerol/water (GW) precursor formulation began with dissolving GMD (30%, *w/v*) and TPO-SDS (1.5%, *w/v*) in a GW solution (50%, *v*/v) under sonication at 45 °C. Then, the solution was mixed with an equal volume of MOFs/GW (1 mg/mL) suspension, followed by the addition of PEGDA (0.5%, *v*/v) and magnetic stirring to ensure a homogeneous precursor solution. The GMD/MOFs-W precursor formulation was prepared using the same procedure, with the GW solvent replaced by deionized water only (W). In addition, GMD-W and GMD-GW precursor formulation were prepared using a similar procedure. For the GMD-W formulation, GMD (15%, *w/v*) and TPO-SDS (0.75%, *w/v*) were dissolved in deionized water, followed by the addition of PEGDA (0.5%, *v*/v) and stirring to homogeneity. By replacing the deionized water described above with GW solution, the GMD-GW precursor formulation was obtained.

2.6. DLP 3D printing

Prior to initiating the printing process, the Materials Test program of DLP 3D printer (MAX X27, Asiga, AUS, wavelength emission 385 nm, nominal *XY* resolution of 27 × 27 μm^2) was used to investigated the functional relationships between light intensity and curing depth, as well as between exposure time and curing depth [32]. The printing parameters for the DLP process were subsequently optimized based on these derived functional models.

3D models were designed using Cinema 4D software and exported as STL files for 3D printing. The DLP process was performed using the Asiga MAX X27 above mentioned. The hydrogels were printed applying pre-optimized parameters, then washed in deionized water (50 °C) or GW solution (depending on their formulation) to remove uncured residues. Subsequently, these hydrogels were post-cured in a UV chamber for 2 min. The obtained GMD/MOFs-GW hydrogel was further immersed in a 0.05 mol/L $FeCl_3$-GW solution at 50 °C for 2 h to allow Fe^{3+} chelation. Finally, the GMD/MOFs/Fe^{3+}-GW hydrogel was stored in a sterile 50% glycerol/PBS (GP) solution at 4 °C to ensure stability until further use.

2.7. Characterization

Structural and morphological characterizations were performed as follows. ^1H NMR spectra of gelatin, GelMA, and GMD were recorded on a nuclear magnetic resonance spectrometer (AVANCE III HD 400, Bruker, Germany) at 400 MHz. UV–vis spectra were collected using a UV–vis spectrophotometer (UV-2600, Shimadzu, Japan) and a multimode microplate reader (BioTek Synergy HTX, Agilent, USA). The chemical structure and crystalline properties were analyzed by Fourier transform infrared spectroscopy (FTIR, NEXUS 470, Nicolet, USA), X-ray diffractometer (XRD, D2 PHASER, Bruker, Germany), and X-ray photoelectron spectroscopy (XPS, AXIS Ultra DLD, Kratos, UK). The micromorphology was observed via a scanning electron microscope (SEM, SU1510, Hitachi, Japan), a field emission scanning electron microscope (FESEM, Regulus8100, Hitachi, Japan), and a transmission electron microscope (TEM, JEM-2100, Hitachi, Japan). For glycerol-containing hydrogels, samples were immersed in deionized water for 24 h (water refreshed every 8 h), lyophilized, and then characterized by FESEM coupled with an energy dispersive X-ray spectroscopy (EDS) system. Particle size statistics were performed using Nano Measurer software (Fudan University, China).

Thermal, mechanical and 3D printing-related characterizations are described below. The thermodynamic behavior of the hydrogels was evaluated by differential scanning calorimetry (DSC, DSC3+, Mettler, Switzerland) over a temperature range of −60 to 60 °C at a heating rate of 10 °C/min. Mechanical performances were characterized by dynamic mechanical analysis (DMA, Q800, TA, USA). Cylindrical 3D-printed hydrogels (diameter = 10 mm, height = 3 mm) were tested between parallel plates (amplitude = 0.05 mm, frequency = 10 Hz) at −40 °C and 37 °C, respectively, to evaluate anti-freezing performance. The photo-rheological behavior of the precursor formulations was measured using a rheometer (Physica MCR 302, Anton Paar, Austria) equipped with a UV spot light source (LC8 lamp, Hamamatsu Photonics, Japan). The uncured formulation was drop-cast onto the center of a quartz platform, and the storage modulus (*G'*) during photopolymerization was recorded in real-time under UV irradiation (40 mW/cm^2) with a 25 mm parallel plate, 0.2 mm gap, 10 Hz frequency, 1% strain, and 30 °C test temperature. The printing fidelity of the 3D printed objects was analyzed using a 3D optical scanner (E3, 3Shape, Denmark). The scanned data were aligned with the original STL model, and the geometric deviations were visualized as a color-coded heat map.

2.8. Visible light transmittance test

A solar power meter (SPM, LH-122, Lianhc, China) was utilized to evaluate the visible light transmittance of 3D printed hydrogels. Before testing, the visible light source was adjusted to achieve a stable irradiance (I_0 = 30 mW/cm^2). A uniformly thick 3D printed hydrogel sample was then placed over the probe, ensuring full coverage. The transmitted light intensity (I) was recorded, and the measurement was repeated 3 times for statistical reliability. The visible light transmittance was calculated using Eq. (1):

$$\text{Visible light transmittance}\ (\%) = \frac{I}{I_0} \times 100 \quad (1)$$

2.9. Adhesion strength test

The skin-adhesion strength of 3D printed hydrogels was evaluated using a standard pull-off adhesion test (ASTM F2258) with fresh porcine skin as the substrate, which closely mimics the properties of human skin [33]. Before testing, porcine skin samples were degreased and surface moisture was removed using filter paper. A 3D printed hydrogel sample (10 × 10 × 1 mm) was sandwiched between two porcine skin layers and maintained at 37 °C for 2 h to ensure sufficient contact. Such skin-hydrogel-skin assembly was subsequently measured using an electronic universal testing machine (PT-1198, Pootab, China) at a constant speed of 5 mm/min until complete detachment occurred. The adhesion strength was calculated according to Eq. (2):

$$\text{Adhesion strength}\ (\text{kPa}) = \frac{F_{max}}{S} \times 1000^{-3} \quad (2)$$

where F_{max} and S represent the maximum tensile force and the adhesion area, respectively.

2.10. Water retention test

Water retention capacity was assessed by exposing hydrogel samples (10 mm diameter, 2 mm thickness) to a controlled dry-heat environment (40 °C, 10% RH). Samples were periodically removed and weighed at predetermined intervals (0.5, 1, 2, 4, 8, 24, 48 h). The weight retention rate was calculated according to Eq. (3):

$$\text{Weight retention rate}\ (\%) = \frac{W_t}{W_0} \times 100 \quad (3)$$

where W_t represents the weight at dehydration time t, and W_0 denotes the initial weight before testing.

2.11. Photodynamic and photothermal activity test

The photodynamic activity was evaluated by ABDA degradation kinetics induced by $^1O_2$. A 3D printed disc-shaped hydrogel sample (diameter = 10 mm, height = 1 mm) was placed at the bottom of a quartz cuvette, followed by the addition of 3 mL ABDA solution (40 mg/L). The system was kept in the dark for 1 h to ensure adsorption

equilibrium. Subsequently, it was exposed to a xenon lamp (~30 mW/cm^2, λ ≥ 420 nm) for 20 min. The UV–vis absorption spectra of the solution were recorded every 5 min using a UV–vis spectrophotometer over a wavelength range of 300–500 nm.

To evaluate the photothermal activity, the disc-shaped hydrogel sample (diameter = 10 mm, height = 1 mm) was irradiated with a xenon lamp (~30 mW/cm^2, λ ≥ 420 nm), and the surface temperature was monitored real-time using an infrared thermal imaging camera (UTi260E, UNI-T, China).

2.12. Antibacterial performance assessments

The antibacterial performance was quantitatively evaluated following a previous method with slightly modification [34]. Gram-positive *Staphylococcus aureus* (*S. aureus*, ATCC 6538) and Gram-negative *Escherichia coli* (*E. coli*, ATCC 43895) were selected as model bacteria in this assay. Specifically, 20 μL of freshly prepared bacterial suspension (10^6 CFU/mL) was pipetted into each well of a sterile 24-well plate, followed by complete coverage with the 3D printed hydrogel samples (diameter = 10 mm, height = 1 mm). The 24-well plate was then irradiated under a Xenon Lamp (30 mW/cm^2, λ ≥ 420 nm) for 15 min, while an identical plate was maintained in darkness as the control. Subsequently, 2 mL of sterile PBS was added to each well, and the bacteria were resuspended by repeated pipetting (10 times). The resuspension was then serially diluted (10-, 100-, and 1000-fold), and 50 μL of each dilution was evenly spread onto LB-agar plates. Bacterial colonies were counted after incubation at 37 °C for 16–24 h. All experiments were performed in triplicate using independent hydrogel samples.

In addition, 200 μL of the bacterial suspension (10^6 CFU/mL) was dropwise pipetted onto LB-agar plates and uniformly spread using a sterile spreader. After the bacterial suspension air-dried naturally, disk-shaped hydrogel samples (diameter = 10 mm, height = 1 mm) were placed onto the inoculated agar plates. Then, the plates were transferred to the Xenon Lamp (30 mW/cm^2, λ ≥ 420 nm) and illuminated for 15 min. Subsequently, the hydrogels were carefully removed with sterile tweezers, and the plates were incubated at 37 °C for 24 h. Herein, GMD-GW samples loaded with 0.5 mg/mL of TH (denoted as GMD/TH-GW) were 3D-printed and served as a release-mediated antibacterial group for comparison.

To further elucidate the bactericidal mechanism of the 3D-printed hydrogels, bacterial suspensions were inoculated onto each hydrogel sample and illuminated for 15 min under the white light (30 mW/cm^2, λ ≥ 420 nm). Then, the treated samples were fixed with 2.5% glutaraldehyde at 4 °C for 24 h, followed by gradient dehydration in ethanol series (50%, 60%, 70%, 80%, 90%, and 100%). After natural drying, the samples were observed by SEM to analyze bacterial morphological changes.

2.13. Hemolysis behavior assessment

A PBS suspension containing 5% (*v*/v) red blood cells (RBCs) was obtained by centrifugation following the previous method [35]. The hemolysis assay was conducted by adding 1 mL of PBS, 40 mg of hydrogel specimen, and 0.5 mL of prepared RBCs/PBS suspension sequentially into a 1.5 mL centrifuge tube. Herein, 1 mL of deionized water and 1 mL of PBS, each mixed with 0.5 mL of RBCs/PBS suspension, were used as the positive and negative controls, respectively. All the mixtures were incubated at 37 °C for 3 h, followed by centrifugation at 2000 rpm for 10 min. After that, a UV–vis spectrophotometer was employed to record the absorbance of each supernatant at 540 nm. The hemolysis ratio was calculated using Eq. (4):

$$\text{Hemolysis ration}\ (\%) = \frac{A_{hydrogel} - A_{negative}}{A_{positive} - A_{negative}} \times 100 \quad (4)$$

where $A_{hydrogel}$, $A_{negative}$, and $A_{positive}$ denote the absorbance values of the hydrogel, PBS, and deionized water groups, respectively.

2.14. Cytotoxicity assessment

The in vitro cytotoxicity of the 3D printed hydrogels on mouse fibroblast cells (L929) was assessed following CCK-8 assay method with leaching pattern [36]. The revied L929 cells were seeded into a 96-well plate and pre-cultured in Dulbecco's Modified Eagle Medium (DMEM) under a 5% CO_2 atmosphere at 37 °C for 24 h. At the same time, 40 mg of sterile hydrogel specimen was immersed in 100 μL of DMEM for extraction. Then, the pre-cultured mediums in 96-well plate were replaced with the same volume of 0.1% Triton X-100, fresh DMEM, and specimen extract, respectively. After an additional 48 h incubation, the CCK-8 reagent was added to each well and incubated for 2 h at 37 °C. The absorbance was measured at 450 nm using a Multimode Reader. Cell viability for each specimen was calculated according to Eq. (5):

$$\text{Cell viability}\ (\%) = \frac{A_{specimen} - A_{positive}}{A_{negative} - A_{positive}} \times 100 \quad (5)$$

where $A_{specimen}$, $A_{positive}$, and $A_{negative}$ represent the absorbance values of the hydrogel specimen, 0.1% Triton X-100 (positive control), and fresh DMEM (negative control), respectively.

The viability of L929 cells was further assessed using a live/dead fluorescence staining assay [37]. Briefly, after co-incubation with 0.1% Triton X-100, fresh DMEM, or specimen extract, the cells in 96-well plate were washed with PBS. Subsequently, a diluted Calcein-AM solution was added and incubated for 15 min in the dark to stain live cells. Following three PBS washes, a diluted propidium iodide solution was added and incubated for 5 min in the dark to stain dead cells. Finally, these cells were rinsed with PBS and imaged under a fluorescence microscope.

2.15. Wound healing assay and histological analysis

Adult male Kunming rats (6–8 weeks old, ~250 g) were used in the wound healing assay. All animal care and experimental procedures were conducted in accordance with the Animal Management Regulations of the Ministry of Health of the People's Republic of China and the Guidelines for the Care and Use of Laboratory Animals in China. The protocols were approved by the Animal Welfare and Ethics Committees of BeiJian Testing Co., Ltd. and Hunan University of Arts and Science. Before the operation, all rats were anesthetized by injection of 4% pentobarbital sodium and fixed in a prone position on a surgical platform. The dorsal hair was shaved and the area was disinfected using povidone-iodine. Then, three full-thickness circular wounds (diameter: ~1 cm) were created on the dorsal skin of each rat, and each wound aera was evenly spread with 50 μL of *S. aureus* suspension (~10^8 CFU/mL). After 60 min of bacterial infection, the three wounds were topically treated with PBS (blank), 3M™ dressing, and GMD/MOFs/Fe^{3+}-GW hydrogel, respectively. Subsequently, the back of rat was irradiated for 15 min with a xenon lamp (~30 mW cm^{-2}, λ ≥ 420 nm), and then covered with sterile gauze. The wound healing progression was recorded at 0, 4, 8, and 12 days, and the wound areas were quantified using ImageJ software. No additional irradiation was performed during the subsequent observation period. The percentage of residual wound area was determined according to Eq. (6):

$$\text{Residual wound area}\ (\%) = \frac{S_n}{S_0} \times 100 \quad (6)$$

where S_n and S_0 denote the wound area on day n and day 0, respectively.

In addition, the wound tissues were harvested from the dorsal region at days 4, 8, and 12 postoperatively following euthanasia. The tissues were fixed in 4% paraformaldehyde solution for 24 h, embedded in paraffin, and sectioned. Subsequently, the histological sections were stained with hematoxylin and eosin (H&E) for further pathological

analysis.

2.16. Statistical analysis

ANOVA and Student's *t*-test were used for statistical analysis. A *P*-value <0.05 was considered statistically significant, while $P > 0.05$ was considered not significant (N. S.). All experimental data were expressed as mean ± standard deviation, with error bars in figures representing standard deviations.

3. Results and discussions

3.1. Characterization of the synthesized GMD and MOFs

The synthetic procedures for GelMA and GMD are illustrated in Fig. S1. Successful synthesis of GMD was verified by chemical structure characterization, with a methacryloyl degree of substitution of ~60% (Figs. S2-S3). Zirconium-based porphyrin-MOFs crystals were synthesized via a hydrothermal method (Fig. S4), and their morphology and crystalline structure were characterized by FESEM and XRD (Figs. S5-S6).

3.2. Design and printability of the 3D-printed formations

In our previous study, the GelMA/MOFs system was shown to be suitable for DLP 3D printing [32]. Herein, the GelMA chains were further functionalized with dopamine moieties and employed as a photocurable precursors for DLP. As displayed in Fig. S7, when water was used as the sole solvent in the formulation (as in the previous protocol), the dopamine-modified GelMA (GMD) exhibited pronounced turbidity upon photocuring. This loss of optical clarity would inevitably reduce the light-harvesting efficiency of the embedded MOFs, with UV–vis absorption spectra (Fig. S8a) showing a marked attenuation of their characteristic absorption peaks. Moreover, the resulting optical scattering markedly diminished the photoinitiation efficiency of internal photosensitizers during DLP 3D printing, ultimately leading to failure in fabricating well-defined architectures (Fig. S8b). After preliminary screening of glycerol concentrations ranging from 20% to 60%, the 50%

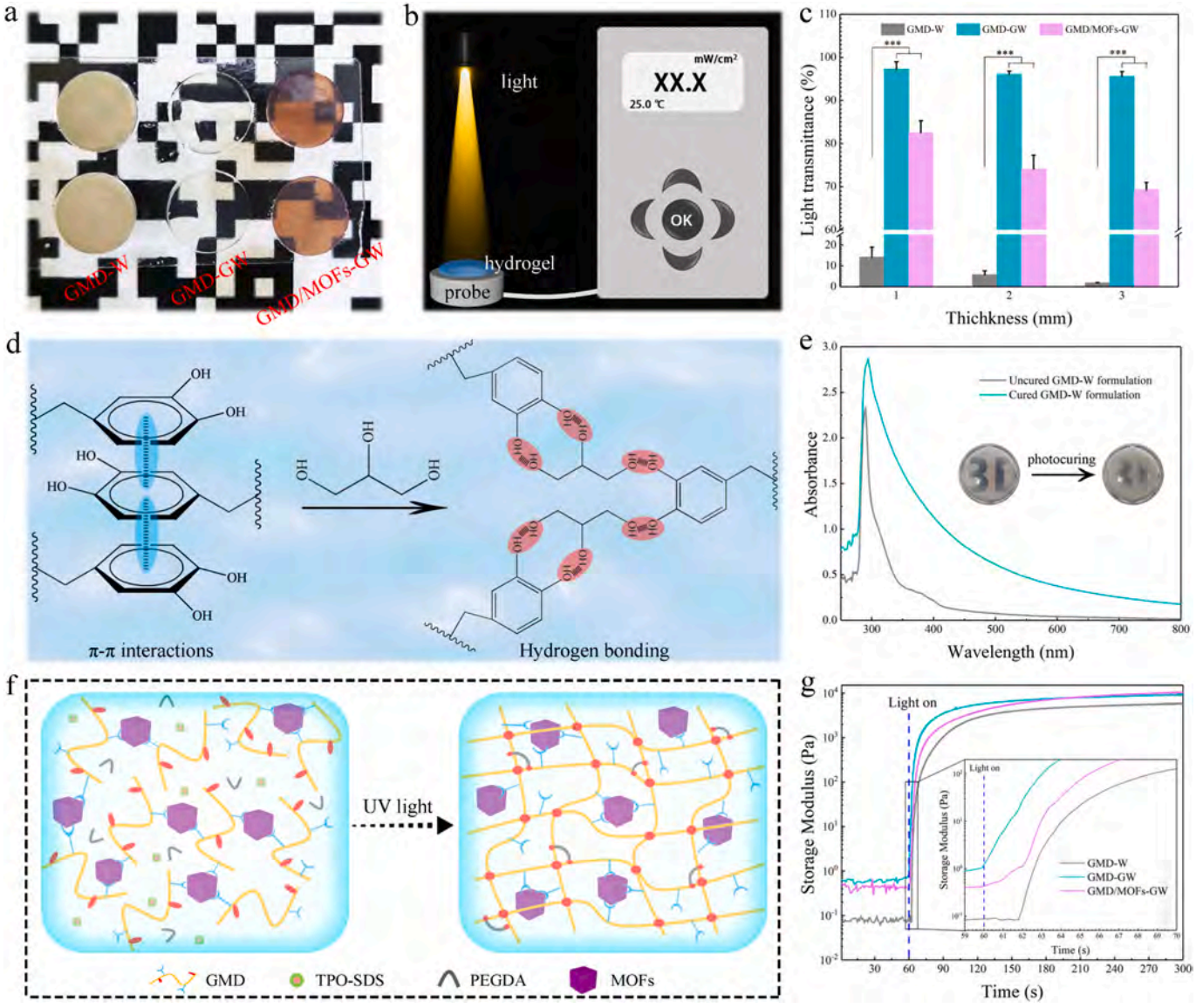


Fig. 1. (a) Optical photographs of GMD-W (left), GMD-GW (middle), and GMD/MOFs-GW (right) hydrogels. (b) Schematic diagram of light transmission measurement. (c) Light transmittance. (d) Schematic diagram of the proposed mechanism for light transmittance improvement. (e) UV–vis spectra of the GMD-W formulation before and after photocuring. (f) Schematic diagram of the crosslinking mechanism for GMD/MOFs-GW hydrogel. (g) Photorheological curves of the given formulations. (*** represents $P < 0.001$).

GW binary system was selected as the optimal formulation. It markedly improved the optical transparency of cured GMD resin, which addressed the turbidity problem and in turn guaranteed sufficient photocuring efficiency and printing feasibility. Fig. 1a presents the photographs of the photocured hydrogels obtained from the GMD-W, GMD-GW, and GMD/MOFs-GW formulations, respectively. The light transmittance of the hydrogels was further quantitatively evaluated using transmission measurements (Fig. 1b). At 1 mm thickness, the GMD hydrogel was largely opaque, with a transmittance of only ~14.2%. In stark contrast, the GMD-GW hydrogel maintained excellent transparency (~97.3%). Notably, even after incorporation of MOFs, the transmittance of the GMD/MOFs-GW hydrogel remained high at ~82.5%. As the thickness increased to 3 mm, the GMD hydrogel became virtually opaque (~1.8% transmittance). Remarkably, the GMD-GW hydrogel retained its transparency (~95.6%), demonstrating negligible thickness-dependent scattering. For the GMD/MOFs-GW hydrogel at this thickness, the transmittance decreased to 69.3%, which could be attributed to the intrinsic absorption and scattering by the embedded MOFs. A proposed mechanism underlying the GW-induced transparency enhancement of the GMD resin is illustrated in Fig. 1d. It is reasonably speculated that in a single aqueous solvent, the catechol groups along the GMD chains tend to form aggregates through π-π stacking. Subsequent photo-crosslinking of methacrylate groups immobilizes these aggregates and may result in irregular chain packing and the formation of large polymer domains, which is a plausible cause for the diminished optical transmittance. [38,39]. Consistently, UV–vis spectroscopy (Fig. 1e) revealed a marked increase in the visible-light absorbance of GMD resin after polymerization in aqueous solvent alone, corroborating the macroscopic decrease in transparency. By contrast, it is proposed that in the GW binary solvent, hydrogen bonding between catechol and glycerol may weaken π-π stacking and facilitate a more uniform chain arrangement, which accounts for the enhanced optical transparency [39]. In addition, the UV–vis absorption spectra of the GMD-GW and GMD/MOFs-GW formulations before and after photocuring are shown in Fig. S9. As expected, the absorption spectra of both GMD-GW and GMD/MOFs-GW formulations exhibited negligible differences before and after photocuring, and the characteristic absorption peaks of MOFs remained distinct, indicating that the optical transparency of the resulting hydrogels was well preserved. In particular, no characteristic absorption peak of ortho-quinone appeared at 395 nm in either cured formulation, confirming that the catechol groups remained unoxidized during the DLP 3D printing [30].

In the printable formulations, 0.5% (*v*/v) PEGDA was used as a crosslinker to improve the printability and structural formability of the hydrogel. This was the lowest concentration of crosslinker that enabled successful printing. Further elevation of the PEGDA content increased the crosslinking density, thereby compromising the flexibility of the hydrogel network. Fig. 1f illustrates the formation mechanism of the GMD/MOFs-GW hydrogel. Following UV exposure, the GMD molecular chains and PEGDA form a three-dimensional network through covalent cross-linking. This network is additionally stabilized Zr^{4+}-catechol coordination with the embedded MOFs, leading to a significant enhancement in structural integrity [40]. Meanwhile, rheological measurements (Fig. S10) demonstrated that the incorporation of MOFs exerted a negligible impact on the viscosity (η) of the formulations, with the η values remaining within the typical range (0.001–1 Pa·s) for conventional DLP 3D printing [41]. Given the potential competitive absorption between the embedded MOFs and the photoinitiator, the photopolymerization kinetics of printing formulations were thoroughly investigated. As shown in Fig. 1g, the polymerization process of GMD-W, GMD-GW, and GMD/MOFs-GW formulations occurred in <10 s upon UV irradiation, which is an indication of their suitability for DLP 3D printing in principle [42]. Theoretically, catechol groups in GMD retard photopolymerization reaction by scavenging free radicals generated by the photoinitiator. However, glycerol in the GW binary system could suppress this retardation by binding to the catechol groups [43]. Consequently, the photorheological results demonstrated an earlier polymerization onset for GMD-GW compared to GMD-W. In contrast, light absorption competition from MOFs moderately delayed the photopolymerization of GMD/MOFs-GW. Such a competitive effect has been strategically exploited in DLP 3D printing to enhance printing fidelity by suppressing undesired polymerization [41].

To further determine the optimal DLP 3D printing parameters, the curing behavior of the GMD/MOFs-GW formulation was investigated using a Materials Test program. As shown in Fig. 2a, curing depth showed a strong linear dependence on exposure time (range: 11–23 s) under constant light intensity, described by the equation $y = -0.33 + 0.06\times$ ($R^2 > 0.99$). Conversely, at a fixed exposure time (Fig. 2b), curing depth exhibited a logarithmic dependence on light intensity (range: 20–40 mW/cm^2), fitted by $y = \ln(0.38 + 0.055\times)$ ($R^2 > 0.95$). These empirical working curves served as the quantitative basis for parameter selection, with the selection criterion set as the cure depth being no less than 1.2 times the layer thickness to ensure reliable interlayer adhesion. For formal printing, a fixed layer thickness of 50 μm was adopted, with a baseline UV intensity of 30 mW/cm^2 and a baseline exposure time of 15 s. Benefiting from the layer-by-layer tunability of the DLP system, the exposure time and light intensity of individual layers were fine-tuned within the calibrated range according to the cross-sectional filling ratio and structural features, to balance curing fidelity and printing efficiency. All parameter adjustments strictly followed the pre-established working curves.

After optimizing the printing parameters, a three-dimensional GMD/MOFs-GW hydrogel structure was fabricated using a DLP 3D printer. The workflow is illustrated in Fig. 2c. A model was first designed with Cinema 4D and exported in STL format, then imported into Asiga Composer for parameter configuration. The photocurable formulation was poured into the resin tank, and the DLP program was initiated. Guided by a high-power UV LED and a high-resolution optical system (27 × 27 μm), the sliced model was projected layer by layer, selectively curing predefined regions. Each cured layer was lifted to allow fresh resin flow, and the process was repeated until a complete 3D hydrogel structure was obtained [44]. Such process enables the fabrication of diverse hydrogel architectures with high structural fidelity. Fig. 2d and e demonstrate that the printed samples faithfully reproduce both the Chinese characters (Jiangnan University) and the English letters (Polito), with smooth surfaces and well-defined edges. The printing accuracy of the GMD/MOFs-GW hydrogel was evaluated using a 3D scanner. As shown in Fig. 2f, the printed hydrogel replicated the original model comprising a circular base and five pyramid-like structures. The geometric deviation heat map reveals that most surface errors were below 0.05 mm, confirming the high fidelity of the printed constructs. Fig. 2g-i exhibited representative 3D models, including bowl, hollow cube and terrain shapes. Notably, a more complex axisymmetric model with central pillars was also accurately reproduced without internal supports (Fig. 2j). The printability achieved is in good agreement with recent literature in the field of photocurable hydrogels with such content of water [32,45–47] and demonstrates the capability of the GMD/MOFs-GW formulation to achieve high-precision replication of intricate structures via DLP 3D printing. Such specific structures are designed to address critical requirements in wound management, including conformability, stretchability, and breathability.

3.3. Characterizations of the 3D-printed hydrogels

Given the catechol groups in GMD molecules, the printed GMD/MOFs-GW hydrogels were subsequently treated with $FeCl_3$ (Fig. S11). Herein, an excess concentration of Fe^{3+} was applied to compensate for diffusion within the hydrogel network, thereby ensuring sufficient catechol-Fe^{3+} coordination. During the treatment, mono catechol-Fe^{3+} complexes were initially formed in the $FeCl_3$-GW solution (pH ~ 2.1) and subsequently converted into bis catechol-Fe^{3+} complexes after immersion in GP solution (pH ~ 7.2). The UV–vis absorption spectra of

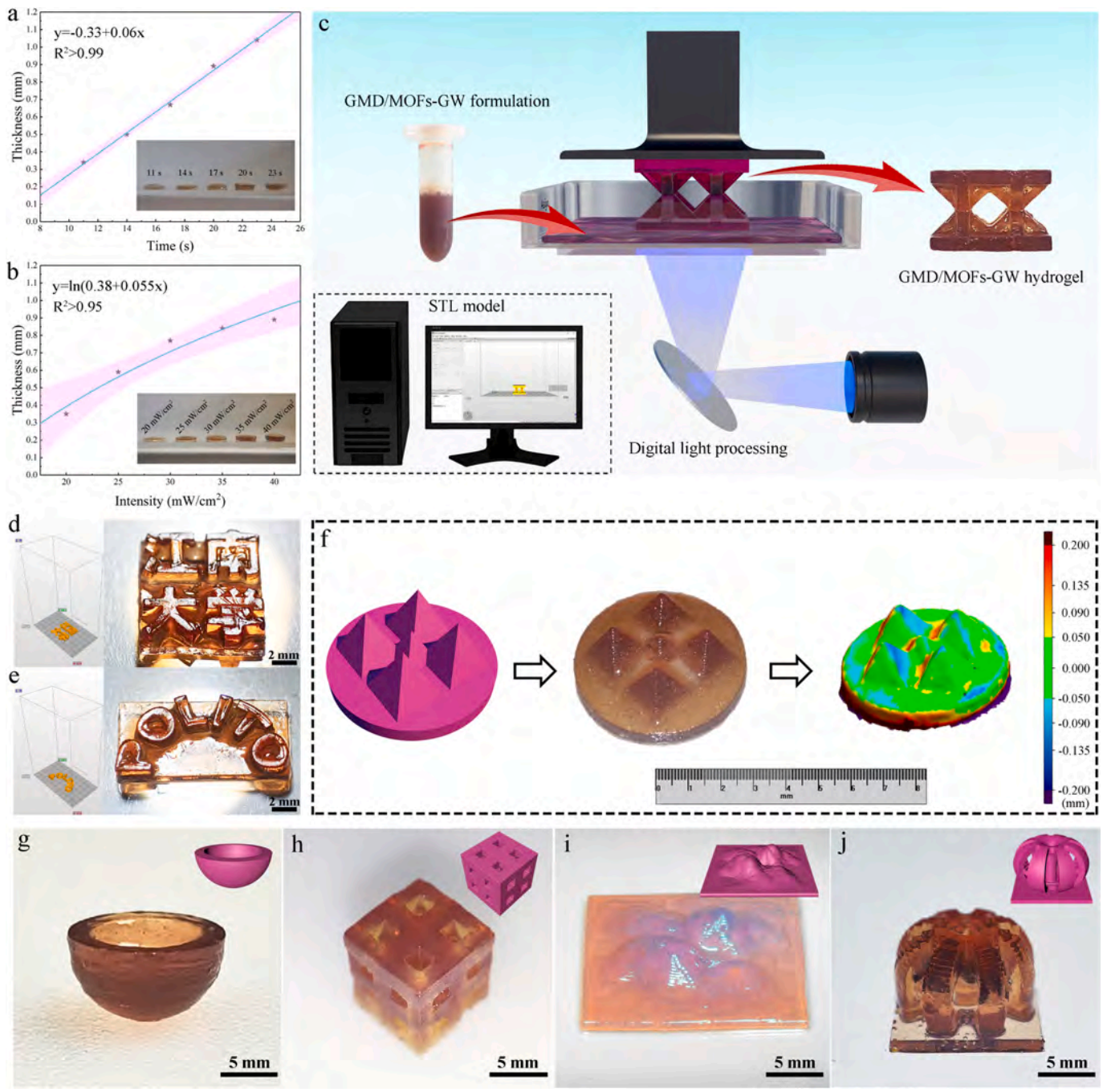


Fig. 2. (a) The functional relationship between curing thickness and exposure time for GMD/MOFs-GW formulation under 40 mW/cm^2 light intensity. (b) The functional relationship between curing thickness and light intensity for GMD/MOFs-GW formulations after exposure for 20 s. (c) Schematic illustration of DLP 3D printing process. (d-e) The STL models and the printed hydrogels of Chinese characters and English letters. (f) Printing accuracy analysis via 3D scanning (Color bar represents deviation from reference, red: positive, blue: negative). (g-j) 3D printed hydrogels with bowl, hollow cube, terrain and axisymmetric structure with central pillar shapes.

different hydrogels are shown in Fig. 3a. The GMD-GW hydrogel exhibited negligible absorption in the visible region. In contrast, the GMD/Fe^{3+}-GW hydrogel displayed a broad absorption band around ~575 nm, which is attributed to the formation of bis catechol-Fe^{3+} complexes [48]. Moreover, in addition to the characteristic peaks of MOFs, the spectrum of the GMD/MOFs/Fe^{3+}-GW hydrogel also exhibited additional features arising from the bis-complex absorption.

To further evaluate the mechanical properties of 3D-printed hydrogels, DMA was performed at physiological temperature (37 °C). As shown in Fig. 3b, the storage modulus (G′) increased from 56.1 kPa for GMD-W to 58.0 kPa for GMD-GW. This increase is consistent with the photorheological results and confirms the reinforcing effect of glycerol. Incorporation of MOFs into GMD-GW further elevated the G′ to 61.7 kPa, indicating a notable enhancement in the crosslinking density and network rigidity. Given the strong chelating affinity between catechol and Zr_6 clusters, the mechanical reinforcement is consistent with catechol-Zr coordination [40]. Following Fe^{3+} treatment, the G′ of GMD/MOFs/Fe^{3+}-GW increased to 72.4 kPa, indicating additional physical crosslinking via bis catechol-Fe^{3+} complexes formation. Therefore, both catechol-MOFs and catechol-Fe^{3+} coordination interactions coexist in the GMD/MOFs/Fe^{3+}-GW hydrogel to improve the mechanical property (Fig. 3c). As shown in Fig. 3d, A compression test

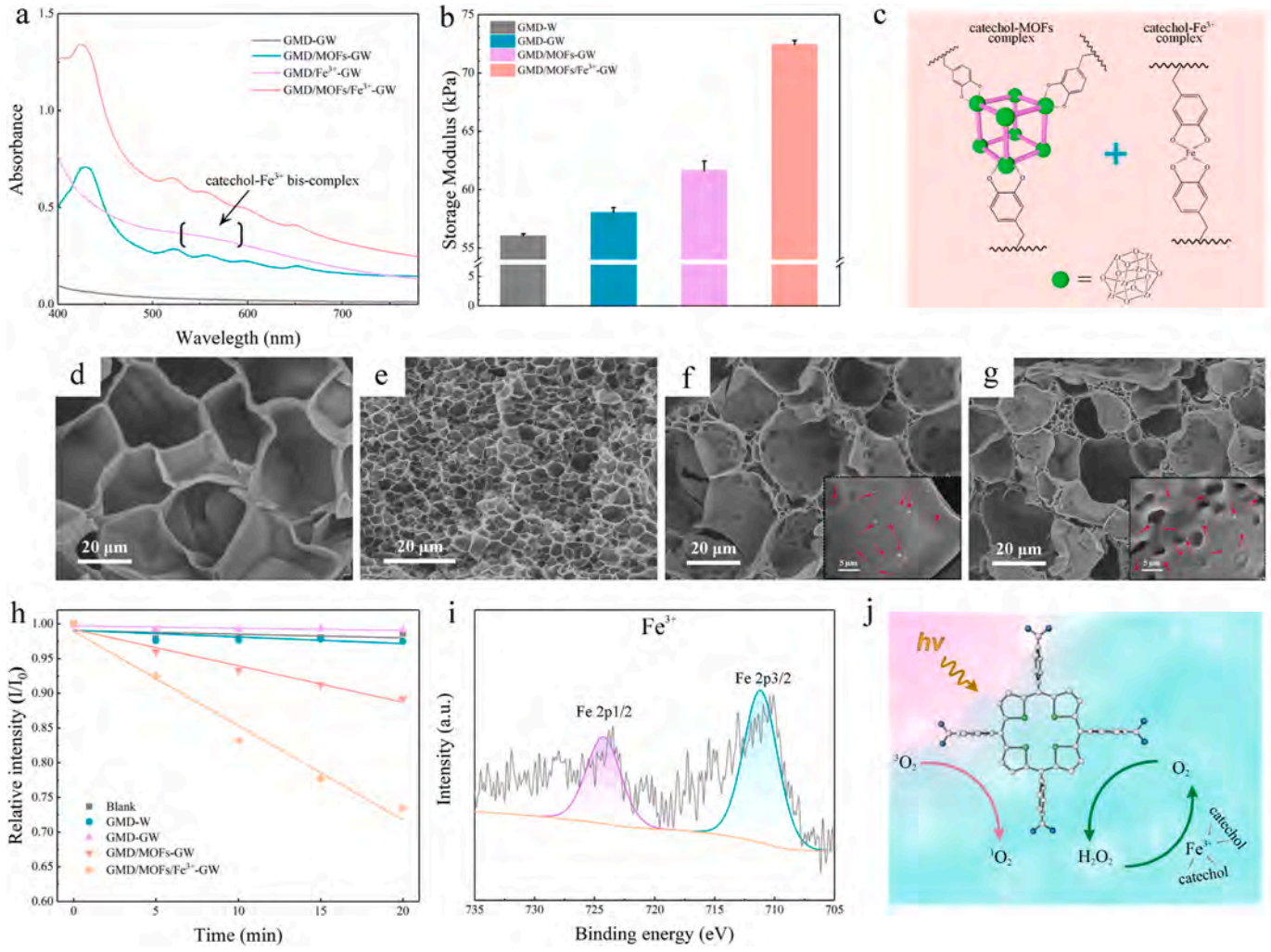


Fig. 3. (a) UV–vis spectra of hydrogels before and after chelating Fe^{3+}. (b) DMA of 3D printed hydrogels at 37 °C. (c) Schematic illustration of catechol-MOFs and catechol-Fe^{3+} complexes. (d-g) SEM images of GMD-W, GMD-GW, GMD/MOFs-GW, and GMD/MOFs/Fe^{3+}-GW hydrogels, respectively. (h) Fitting curves of ABDA degradation rate. (i) Fe 2p XPS spectrum of GMD/MOFs/Fe^{3+}-GW. (j) Schematic diagram of the proposed mechanism for $^1O_2$ generation enhancement.

was conducted to further evaluate the mechanical robustness of the 3D-printed circular GMD/MOFs/Fe^{3+}-GW hydrogel (Video 1). The circular hydrogel exhibited remarkable fracture resistance and efficient deformation recovery, which can be attributed to the synergistic contribution of covalent bonds, hydrogen bonds, and dual coordination interactions. Notably, the mechanical performance measured are slightly higher than similar systems without MOFs, underscoring the importance of matrix/filler interaction. [49]

Fig. 3d-g presents SEM images of freeze-dried 3D-printed hydrogels. Prior to lyophilization, the GMD-GW, GMD/MOFs-GW, and GMD/MOFs/Fe^{3+}-GW hydrogels were immersed in deionized water to remove glycerol. All freeze-dried hydrogels exhibited porous morphologies in these images. Compared with GMD-W, the GMD-GW hydrogel showed smaller pore sizes. This was attributable to the partial retention of glycerol, which formed hydrogen bonds with GMD, as only partial removal occurred during solvent exchange. In GMD/MOFs-GW and GMD/MOFs/Fe^{3+}-GW, both large and small pores were observed, reflecting a heterogeneous network architecture. This morphology is ascribed to the incorporation of MOFs and Fe^{3+}, which facilitated the formation of metal-coordination complexes, thereby inducing heterogeneous chain migration and rearrangement of GMD molecules during freeze-drying [50]. Furthermore, high-magnification FESEM images in Fig. 3f and g revealed small surface protrusions on GMD/MOFs-GW and GMD/MOFs/Fe^{3+}-GW, which are attributed to embedded insoluble MOF crystals. The EDS spectrum (Fig. S12a) confirmed the presence of all constituent elements, and the corresponding elemental mapping (Fig. S12b) demonstrated a uniform spatial distribution of Zr and Fe.

The photodynamic activity of the MOF-embedded 3D-printed hydrogels was assessed using ABDA as a $^1O_2$ probe. The absorption spectrum of ABDA alone remained essentially unchanged after 20 min of irradiation (Fig. S13a), confirming its stability under the applied light. Similarly, ABDA solutions containing GMD-W or GMD-GW hydrogels exhibited negligible spectral variations (Fig. S13b and c), indicating a lack of photodynamic activity in these systems. In sharp contrast, a pronounced decrease in absorbance at the characteristic peak was observed in the presence of GMD/MOFs-GW and GMD/MOFs/Fe^{3+}-GW hydrogels (Fig. S14a and b). This observation is attributable to the degradation of ABDA by $^1O_2$ generated from the hydrogels upon irradiation. To further quantify the $^1O_2$ generation efficiency, the photodegradation rate of ABDA was analyzed based on the absorbance decrease at 400 nm (Fig. 3h). The slope values obtained from linear fitting for the control, GMD-W, and GMD-GW groups approximated zero, verifying their negligible photodynamic activity. Conversely, the GMD/MOFs-GW and GMD/MOFs/Fe^{3+}-GW groups exhibited distinct photodegradation kinetics, with fitted slopes of -5.25×10^{-3} and -1.36×10^{-2}, respectively. These findings demonstrate the efficient light-induced $^1O_2$ generation of MOF-embedded 3D-printed hydrogels. Moreover, the efficiency of GMD/MOFs/Fe^{3+}-GW was

approximately 2.6-fold higher than that of GMD/MOFs-GW, thereby confirming its significant enhancement effect. To elucidate the mechanism underlying this enhancement, XPS analysis was performed on the dried hydrogel (Fig. 3i). The results showed Fe^{3+} (711.2 and 724.4 eV) existed in a stable complexed state within the hydrogel matrix [51,52]. In addition, linear fitting of H_2O_2 detection profiles demonstrated negligible H_2O_2 release from the GMD/MOFs/Fe^{3+}-GW hydrogel under illumination, while the GMD/MOFs-GW hydrogel displayed prominent H_2O_2 release (Fig. S15). Thus, we propose that the photoexcited porphyrin units in MOFs react with oxygen via two distinct pathways—energy transfer and electron transfer—generating $^1O_2$ and H_2O_2, respectively [53,54]. The stably retained Fe^{3+} ions rapidly catalyze the decomposition of photogenerated H_2O_2 to regenerate oxygen through the catalase-like reaction [55]. This photocatalytic oxygen cycling not only suppresses H_2O_2 accumulation, thereby limiting the electron transfer pathway, but also increases the local oxygen concentration, promoting the energy transfer route and consequently enhancing the yield of highly targeted $^1O_2$ (Fig. 3j). To confirm the light-dependent nature of such photo-reaction, ABDA degradation was tested with GMD/MOFs-GW and GMD/MOFs/Fe^{3+}-GW hydrogels in the dark (Fig. S16). The absence of any degradation confirms that the photodynamic effect is triggered only upon illumination.

Porphyrin-MOFs and Fe^{3+} ions are well recognized as efficient photothermal agents [56,57]. The photothermal performance of the 3D-printed hydrogels was recorded under visible light irradiation. As shown in Fig. 4a, all hydrogels exhibited a temperature rise during 30 min of illumination, with GMD/MOFs-GW and GMD/MOFs/Fe^{3+}-GW showing the most pronounced heating, reaching 50.8 °C (ΔT = 26.4 °C) and 61.4 °C (ΔT = 37.0 °C), respectively. In contrast, GMD-W and GMD-GW showed only minor temperature increases to 33.2 °C (ΔT = 8.8 °C) and 35.5 °C (ΔT = 11.1 °C). Infrared thermal images captured within the initial 5 min (Fig. 4b) further revealed the fast surface heating of GMD/MOFs-GW and GMD/MOFs/Fe^{3+}-GW, with the latter exhibiting superior performance. The cyclic photothermal stability (Fig. 4c) showed that

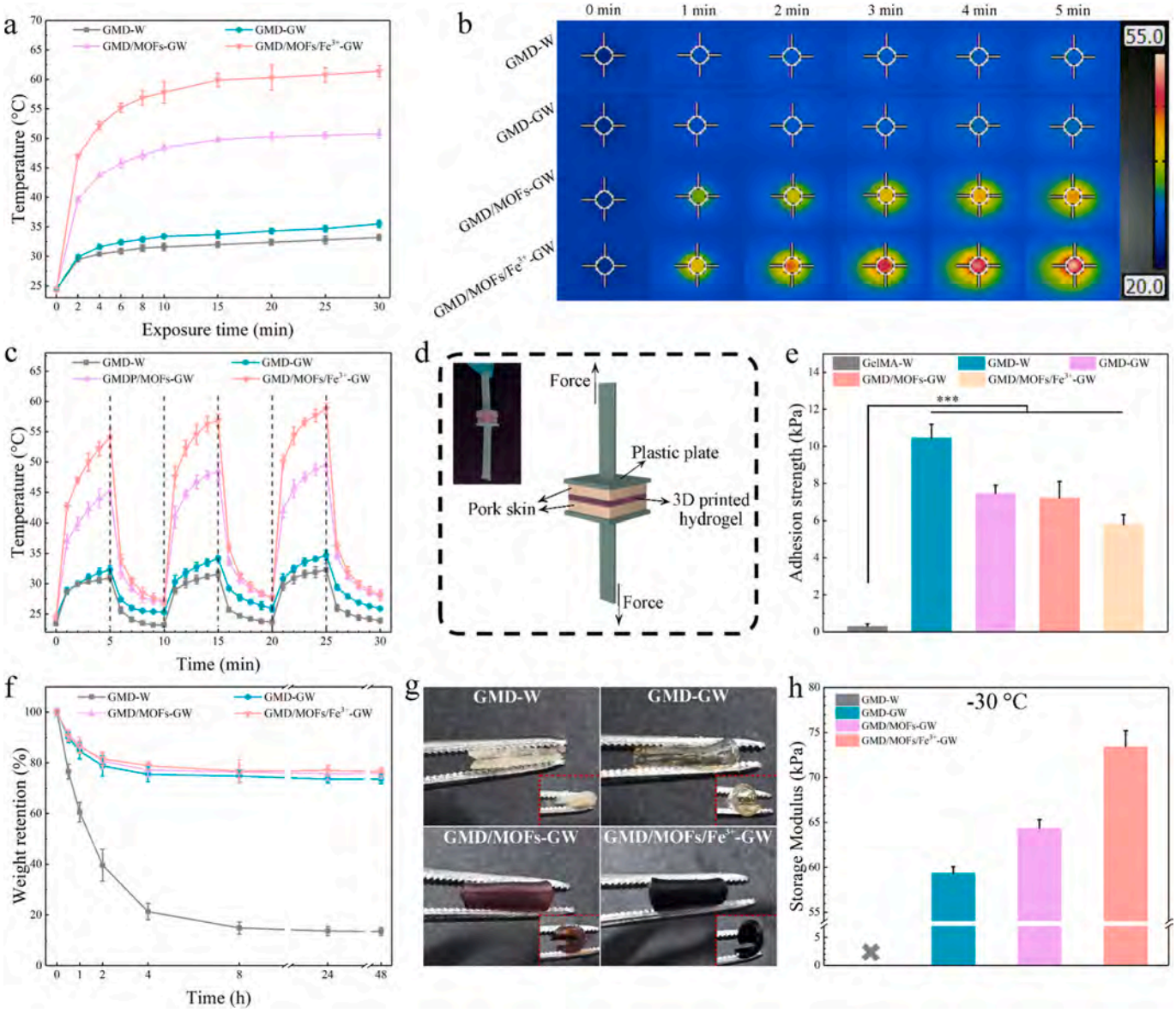


Fig. 4. (a) Heating curves of GMD-W, GMD-GW, GMD/MOFs-GW and GMD/MOFs/Fe^{3+}-GW hydrogels under light illumination within 30 min. (b) Thermal images of hydrogel samples under light illumination within 5 min. (c) Heating-cooling curves of GMD-W, GMD-GW, GMD/MOFs-GW and GMD/MOFs/Fe^{3+}-GW hydrogels under cyclic light illumination. (d) Schematic illustration of tensile-adhesion test. (e) Adhesion strength of different hydrogels to the pork skin. (f) Weight retention of the hydrogels stored at 40 °C with 10% relative humidity for 48 h. (g) Photographs of each hydrogel with bending after being frozen at −30 °C for 24 h. (d) DMA of each hydrogel at −30 °C.

both hydrogels underwent rapid heating and cooling during repeated on/off light cycles, maintaining excellent repeatability. Notably, the maximum temperature in each cycle slightly increased, likely due to gradual water loss and enhanced thermal conductivity. Quantitatively, the maximum temperature rise of GMD/MOFs/Fe^{3+}-GW under visible light irradiation was approximately 1.4 times that of GMD/MOFs-GW. These findings confirm that MOFs endow the hydrogel with outstanding photothermal properties, while Fe^{3+} acts as a synergistic component to further enhance the photothermal heating effect.

Catechol groups in GMD molecular chains enable strong adhesion to biological tissues through hydrogen bonding and cation-π interactions with surface functional groups [58,59]. Hence, we evaluated the tissue adhesion strength of 3D-printed hydrogels on porcine skin (simulating human tissue) using a tensile-adhesion test (schematic, Fig. 4d). As shown in Fig. 4e, GelMA-W, which lacks catechol groups, exhibited minimal adhesion (~0.29 kPa). In contrast, GMD-W showed significantly stronger adhesion (~10.45 kPa), attributed to its abundant catechol groups. The adhesion strengths of GMD-GW, GMD/MOFs-GW, and GMD/MOFs/Fe^{3+}-GW were lower, at approximately 7.46 kPa, 7.20 kPa, and 5.79 kPa, respectively. This gradual decrease suggests that glycerol, MOFs, and Fe^{3+} each interact with catechol groups, likely reducing adhesion through two mechanisms: (1) increased internal crosslinking that restricts polymer chain mobility at the interface, and (2) partial blocking of accessible catechol groups, limiting their interaction with the tissue surface [59].

The applicability of hydrogel dressings under extreme conditions remains a key challenge for their practical translation. Most conventional hydrogels are prone to dehydration in dry environments or freezing at low temperatures, compromising their structural integrity and functionality, thus severely limiting their potential for medical use in harsh scenarios [60]. In this work, glycerol and water molecules self-assembled into a stable hydrogen-bonded network, which not only preserved water activity but also significantly suppressed evaporation and permeation, thereby ensuring long-term hydration stability. As shown in Fig. 4f, after 48 h under arid conditions (40 °C, 10% RH), the GMD-W hydrogel retained only ~13.5% of its mass, indicating severe dehydration. In contrast, the hydrogels incorporating the GW system (~39% theoretical water content) retained ~75% of their mass. This difference is attributed to the effective water-retention capability imparted by glycerol. As displayed in Fig. S17, the GMD-W hydrogel shrank drastically (> 78%), becoming dry and rigid after 48 h, whereas the GW-system hydrogels maintained their volume with <24% shrinkage due to limited water loss. This excellent shape stability is critical for extending the service life of hydrogel dressings under arid conditions. In addition to preventing drying, glycerol confers antifreeze properties to the hydrogels by disrupting hydrogen bonds between water molecules and inhibiting ice crystal formation [61]. As shown in the DSC curves (Fig. S18), the GMD-W hydrogel exhibits an endothermic peak near 3.4 °C, corresponding to ice melting. However, the peaks for the GMD-GW, GMD/MOFs-GW, and GMD/MOFs/Fe^{3+}-GW hydrogels are all shifted to around −35.8 °C, indicating that the GW binary solvent system significantly depresses the freezing point and enhances antifreezing performance. Fig. 4g exhibits the bending states of the hydrogels after storage at −30 °C for 24 h. The GMD-W hydrogel fractured during bending, while the other three showed excellent flexibility without any cracks. As shown in Fig. 4f, the frozen GMD-W hydrogel had an impractically high storage modulus, and the GW-based hydrogels showed increased moduli compared to those at 37 °C, due to suppressed polymer chain dynamics [47,62]. The above findings confirm that the GW binary solvent system endows the 3D-printed hydrogels with excellent anti-freezing and water-retention capabilities, making them suitable for use in extreme conditions.

3.4. Antibacterial efficacy and biocompatibility of 3D-printed hydrogels

The antibacterial performance was evaluated given the promising photodynamic and photothermal activities of the GMD/MOFs/Fe^{3+}-GW hydrogels. As shown in Fig. 5a and b, the blank control showed that 15-min light irradiation alone resulted in negligible reductions of *S. aureus* (~29.22%) and *E. coli* (~18.89%), indicating no meaningful bactericidal capacity of the light. Similarly, the GMD-GW hydrogel showed no significant antibacterial activity under either dark or light conditions, confirming its lack of inherent antimicrobial properties. However, the incorporation of MOFs dramatically boosted the antibacterial efficiency of the hydrogel under light irradiation. Specifically, the GMD/MOFs-GW hydrogel achieved high antibacterial efficiencies (~99.83% and ~ 99.82% against *S. aureus* and *E. coli*, respectively). This performance was further enhanced by GMD/MOFs/Fe^{3+}-GW hydrogel, yielding a 99.99% eradication rate against both strains. Moreover, neither of the MOFs-embedded hydrogels exhibited significant antibacterial efficacy in the dark, confirming the photodynamic/photothermal nature of their bactericidal action and its intrinsic dependence on light activation. This visual evidence is directly supported by representative images of the bacterial growth on agar plates (Fig. 5a).

The bactericidal mechanism was investigated by examining the morphological changes of both bacterial strains via SEM after they were incubated on the hydrogels and irradiated for 15 min. As shown in Fig. 5d, both *S. aureus* and *E. coli* on the GMD/-GW hydrogel exhibited intact and regular morphologies, whereas those on the GMD/MOFs-GW and GMD/MOFs/Fe^{3+}-GW hydrogels showed notable deformation and rupture. This phenomenon is attributed to the efficient PDT/PTT inactivation mechanism. Specifically, upon irradiation, the MOF-embedded hydrogels generate cytotoxic $^1O_2$ and localized heat, thereby collectively disrupting bacterial membrane integrity and physiological functions to induce lethal outcomes [63,64].

Typically, the transient nature of $^1O_2$ and poor thermal conductivity confine the bactericidal activity of PDT/PTT hydrogels to a localized area [65]. Therefore, we conducted an inhibition zone assay to investigate the bactericidal mode of the GMD/MOFs/Fe^{3+}-GW hydrogels. As shown in Fig. 5e, *S. aureus* and *E. coli* colonies in the blank group grew uniformly on the agar plates, indicating that the illumination conditions had no interfering effect on the experimental results. In the release-mediated antibacterial group, distinct inhibition zones around GMD/TH-GW hydrogels stemmed from TH diffusion that generates a bactericidal microenvironment to inhibit bacterial growth [66]. In the absence of TH, the GMD-GW hydrogels reduced bacterial colonies only underneath them, with no detectable inhibition zone in the surrounding area. This observed reduction is more likely attributable to physical adhesion rather than direct killing. Notably, the GMD/MOFs/Fe^{3+}-GW hydrogels achieved near-complete bacterial inactivation within the covered area, confirming the robust killing efficacy of the integrated PDT/PTT. The absence of an inhibition zone around the hydrogel, combined with the short diffusion range of $^1O_2$ and the immobilization of photoactive components in the network, suggests that the bactericidal effect is predominantly contact-mediated. Accordingly, DLP 3D printing offers a practical therapeutic advantage by enabling precisely fitted hydrogel dressings, which ensures close tissue contact favorable for treatment efficacy. This role of 3D printing was recently reported in literature for different hydrogel systems. [46,47]

To verify the critical role of the GW antifreeze system in preserving photodynamic antibacterial activity at extreme low temperatures, a glycerol-free aqueous hydrogel (GMD/MOFs/Fe^{3+}-W) was obtained via solvent exchange, which fully froze at −30 °C. As shown in Fig. S19a, the frozen GMD/MOFs/Fe^{3+}-W hydrogel achieved only ~39.34% (*S. aureus*) and ~ 55.63% (*E. coli*) bacterial reductions under light irradiation at −30 °C, while the GMD/MOFs/Fe^{3+}-GW hydrogel retained an exceptional 99.99% bactericidal efficiency under identical conditions. This result is ascribed to the severe inhibition of $^1O_2$ diffusion induced by ice formation in frozen hydrogels, whereas the GW binary system maintains a continuous liquid phase within the 3D-printed GMD/MOFs/Fe^{3+}-GW hydrogel network, thereby providing the essential medium for $^1O_2$ transport and antibacterial activity at this extremely

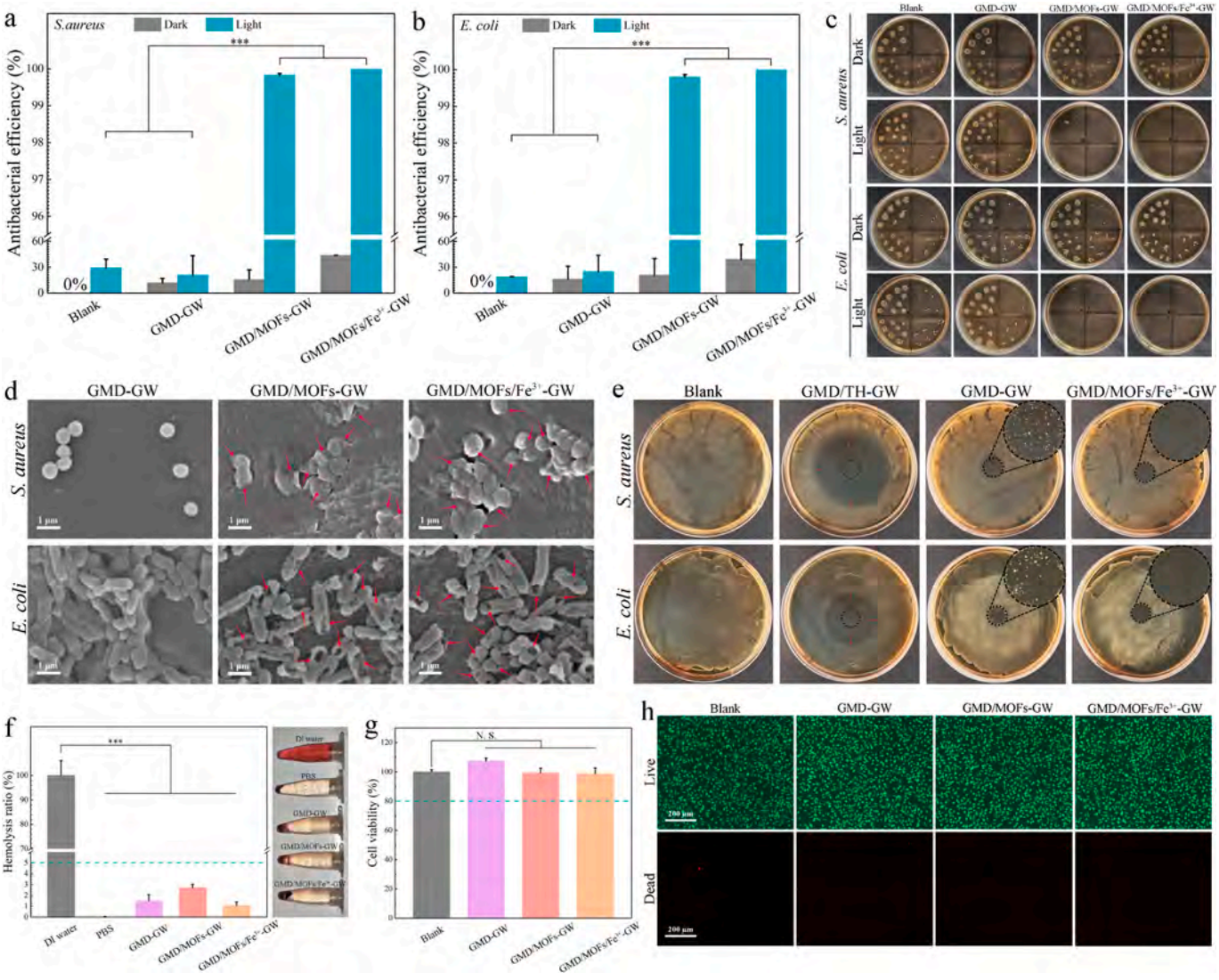


Fig. 5. Antibacterial efficiency of different hydrogels against (a) *S. aureus* and (b) *E. coli.* (c) Survival colonies of bacteria after the antibacterial testing. (d) SEM images showing the bacterial morphology on the surface of hydrogels after 15 min light illumination. (e) Inhibition zone assay for evaluation of bacterial killing mode. (f) Hemolysis ratios and photographs of hemolysis results. (g) Cytocompatibility evaluation. (h) Live/dead staining images of L929 cells. (*** and N. S. represents $P < 0.001$ and $P > 0.05$, respectively).

low temperature [67].

The hemocompatibility and cytocompatibility of the 3D-printed hydrogels were evaluated using in vitro hemolysis and cytotoxicity assays, respectively. As shown in Fig. 5f, deionized water (positive control) induced a hemolysis ratio close to 100%, which was visually confirmed by the near-total disruption of RBCs in the corresponding inset. Conversely, the PBS solution (the negative control) resulted in a hemolysis ratio of nearly 0%, with the RBCs remaining intact and no significant hemolysis observed. Notably, the hemolysis ratios of the GMD-GW, GMD/MOFs-GW, and GMD/MOFs/Fe^{3+}-GW hydrogels (approximately 1.5%, 2.7%, and 1.0%, respectively) were all well below the established safety threshold of 5% [68]. Furthermore, the corresponding insets showed that the RBCs largely maintained their structural integrity with no obvious hemolysis, demonstrating their excellent hemocompatibility. The cytotoxicity results are presented in Fig. 5g. The cell viability of the GMD-GW, GMD/MOFs-GW, and GMD/MOFs/Fe^{3+}-GW hydrogels were approximately 107.4%, 99.3%, and 98.7%, respectively. All values exceeded the safety standard of 80%, demonstrating no significant cytotoxicity for such three hydrogels [69]. Fig. 5h further shows the fluorescence staining images of L929 cells after co-culture with these hydrogels. It can be observed that the majority of cells in all groups exhibited green fluorescence, indicating that they were viable and maintained a healthy, normal morphology. Only a minimal number of cells displayed red fluorescence, signifying a dead state. This observation is fully consistent with the quantitative cell viability results. Therefore, these findings from in vitro hemolysis and cytotoxicity assays confirm that the 3D-printed GMD-GW, GMD/MOFs-GW, and GMD/MOFs/Fe^{3+}-GW hydrogels possess excellent biocompatibility and meet the essential non-toxicity requirements for medical wound dressings.

3.5. Evaluation of wound healing performance

To assess the in vivo PDT/PTT therapeutic potential of 3D-printed hydrogels, we established a *S. aureus*-infected rats' dorsal wound model and selected GMD/MOFs/Fe^{3+}-GW hydrogels for treatment (Fig. 6a). Fig. 6b shows the wound healing processes treated with PBS, 3M™, and the GMD/MOFs/Fe^{3+}-GW hydrogels over 12 days. It was obvious that the GMD/MOFs/Fe^{3+}-GW group exhibited faster wound contraction more vigorous peri-wound hair regrowth, indicating accelerated recovery of the infected-wound and surrounding skin. As shown in Fig. 6c, the residual wound area in all groups gradually reduced, a trend consistent with the expected action of the body's inherent

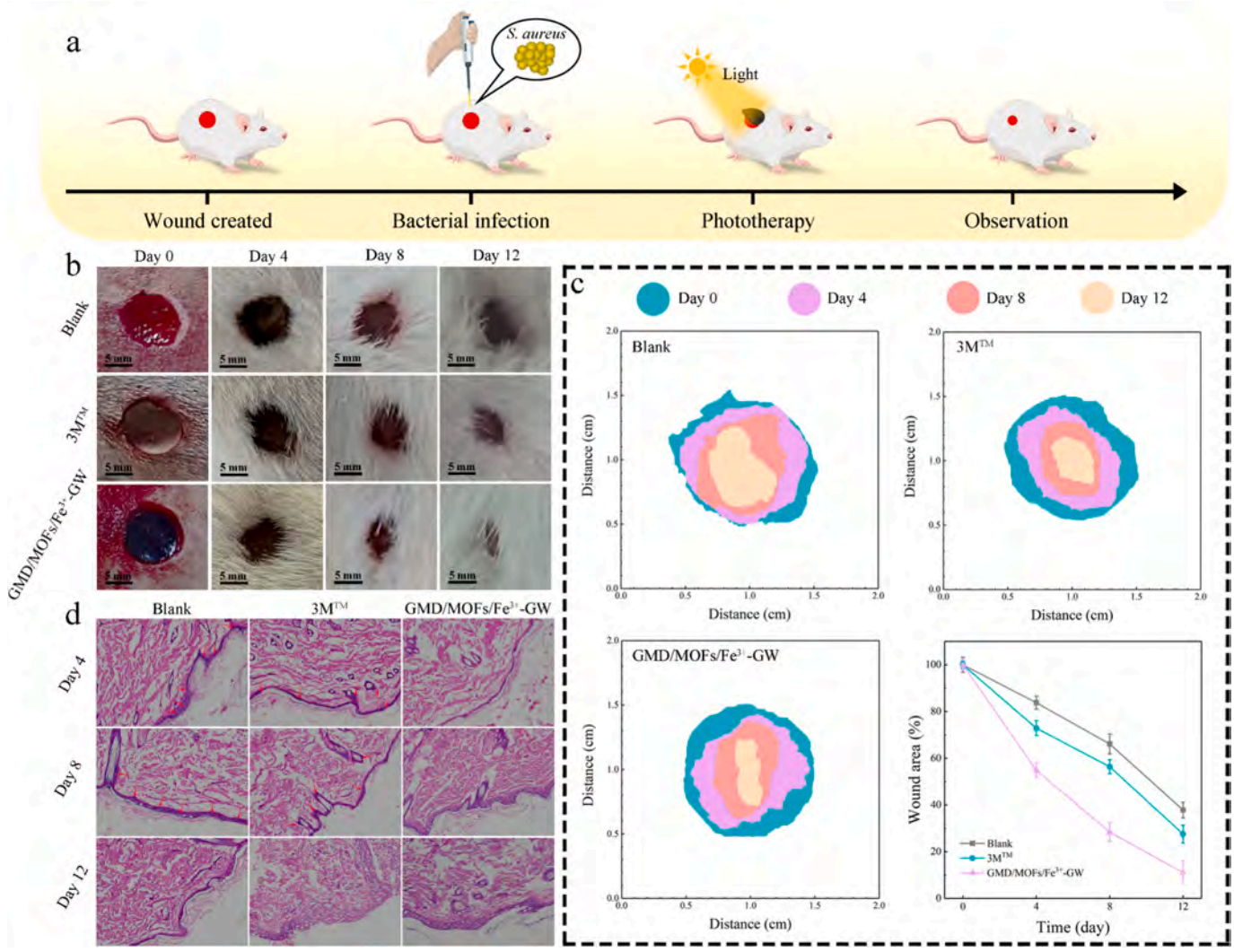


Fig. 6. (a) Schematic diagram of therapeutic strategy for *S. aureus* infected wounds. (b) Photographs of wound healing at days 0, 4, 8, 12. (c) Wound area simulation and calculation at days 0, 4, 8, 12. (d) H&E staining of wound sites at days 4, 8, 12.

immunity and self-recovery [70]. The blank group exhibited the largest residual area on days 4, 8, 12, with wound closure rates of 16.2%, 33.9%, 62.2%, respectively. The commercial 3M™ dressing improved healing efficiency, with rates of 27.1%, 43.6%, 72.5% on the same days. Notably, the GMD/MOFs/Fe^{3+}-GW hydrogel achieved the highest rates (45.1%, 71.7%, 89.0%) on days 4, 8, 12.

H&E staining was further employed to assess histopathological changes during wound healing. As depicted in Fig. 6d, substantial inflammatory cells (red arrows) were present in the blank and 3 M™ groups on day 4, while significantly fewer were observed in the GMD/MOFs/Fe^{3+}-GW group. This indicates that the potent PDT/PTT activity of GMD/MOFs/Fe^{3+}-GW hydrogel effectively controlled infection and relieved inflammation. By day 8, the GMD/MOFs/Fe^{3+}-GW group showed complete resolution of inflammation and early re-epithelialization, while inflammatory cells were still evident in the blank and 3M™ groups. At day 12, inflammation had subsided and epidermal regeneration was complete across all groups, with the formation of new hair follicles observed only in the GMD/MOFs/Fe^{3+}-GW group. Neo-epidermal thickness was quantified to assess re-epithelialization across treatment groups (Fig. S20). At day 4, all groups showed similarly thin neoepidermis (~15–18 μm) corresponding to early-stage wound repair. By day 8, the GMD/MOFs/Fe^{3+}-GW group exhibited substantially higher neoepidermal thickness (~36.5 μm) than the blank (~25.4 μm) and commercial 3 M™ dressing (~20.6 μm) groups. Persistent bacterial infection in the blank group suppressed epithelial maturation, resulting in stagnant and slightly reduced neo-epidermal thickness (~23.4 μm) at day 12. Despite delayed epithelial growth at day 8, the 3M™ group improved to ~47.7 μm by day 12. Notably, the GMD/MOFs/Fe^{3+}-GW hydrogel achieved the greatest neoepidermal thickness (~53.1 μm) at day 12, approaching native rat epidermal thickness. These findings confirm that this phototherapeutic hydrogel potently promotes epithelial regeneration in infected wounds, and are in good agreement with recent literature. [47] Nevertheless, further experiments are required to better evaluate the efficacy of the proposed material in vivo testing, which will be investigated in a dedicated follow-up study. In particular it would be necessary to conduct a full campaign of comparative studies with dedicated control experiments which can describe the role of every single component.

To objectively evaluate the performance of this work, a multidimensional comparison with representative hydrogel wound dressings reported in literature was performed (Fig. S21). The comparative analysis based on actual available literature reveals that our hydrogel has unique advantages in printing precision, extreme low-temperature resistance and antibacterial efficacy, while its mechanical property and wound healing rate are relatively moderate compared with specially optimized systems.

4. Conclusions

Collectively, this work establishes an innovative paradigm for advanced wound management by synergizing rational hydrogel design with DLP-based additive manufacturing. The strategic incorporation of glycerol enhances printability, optical transparency, and environmental stability of the hydrogel. Meanwhile, the dual coordination networks (catechol-MOFs and catechol-Fe^{3+}) represent a unique design strategy that simultaneously optimizes mechanical robustness (storage modulus ~72.4 kPa at 37 °C). Fe^{3+}-mediated amplification of photodynamic (~2.6-fold increase in $^1O_2$ yield) and photothermal (~1.4-fold increase in maximum temperature rise) performance enables potent antibacterial activity, achieving 99.99% inactivation of *S. aureus* and *E. coli* within 15 min. In vivo validation demonstrates clinically significant wound healing efficacy (~89.0% healing rate at 12 days vs. 72.5% for commercial dressings), with effective inflammation suppression. Beyond traditional wound dressings, the DLP manufacturing approach provides unprecedented design freedom, enabling patient-specific morphology matching and programmable internal architectures for integrating sensors or therapeutic devices. This convergence of advanced coordination chemistry, functional biomaterials, and digital manufacturing technology opens new avenues for personalized medicine, with broader implications extending to tissue engineering, wearable bioelectronics, and next-generation theranostic platforms.

CRediT authorship contribution statement

Yang Wang: Writing – original draft, Investigation. **Qufu Wei:** Writing – review & editing, Supervision. **Francesca Frascella:** Writing – review & editing, Supervision. **Cesare Gabriele Gaglio:** Writing – review & editing, Investigation. **Candido Fabrizio Pirri:** Writing – review & editing, Resources. **Xiaoli Jia:** Writing – review & editing, Investigation. **Anguo Xiao:** Writing – review & editing, Resources. **Ignazio Roppolo:** Writing – original draft, Supervision, Methodology, Conceptualization.

Ethical statement

The experimental operations in this study strictly complied with the appropriate ethical guidelines. All animal experiments were approved by the Institutional Animal Care and Use Committee (IACUC) at Hunan University of Arts and Science (approval number: HNWL-HXYCLGC-18).

Declaration of competing interest

The authors declare that they have no known competing financial interests or personal relationships that could have appeared to influence the work reported in this paper.

Acknowledgments

This work is supported by the Start-up Foundation for Doctors of Hunan University of Arts and Science (No. 25BSQD49), the Research Program of Hunan University of Arts and Science (No. 24YB05), Key Research and Development Program of Changde (No. CDKJJ20253406), and the College Students' Innovation and Entrepreneurship Training Program of Hunan Province (No. 202510549021). We also appreciate the support from China Scholarship Council (No. 202206790041).

Appendix A. Supplementary data

Supplementary data to this article can be found online at https://doi.org/10.1016/j.bioadv.2026.215255.

Data availability

Data are reported in the manuscript or in the supporting information file

References

[1] Z. Jiang, J. Feng, F. Wang, J. Wang, N. Wang, M. Zhang, C.Y. Hsieh, T. Hou, W. Cui, L. Ma, AI-guided design of antimicrobial peptide hydrogels for precise treatment of drug-resistant bacterial infections, Adv. Mater. 37 (20) (2025) 2500043.
[2] Q. Ding, Y. Xie, K. Xiong, H. Jia, L. Chen, C. Li, Q. Yi, P. Zhang, L. Mei, B.Z. Tang, From light to cure: precision phototherapies for antibiotic-refractory biofilm infections, Angew. Chem. Int. Ed. 64 (43) (2025) e202510900.
[3] Y. Chen, D. Li, X. Chen, D. Wang, Y. Huang, Y. Gao, F. Liu, X. Lin, D. Zhao, J. Ji, D. Wang, Q. Jin, Side-chain engineering of NIR-II-emissive aggregation-induced emission luminogens to boost photodynamic and photothermal antimicrobial therapy, ACS Nano 19 (16) (2025) 16147–16162.
[4] W. Lu, Z. Fang, X. Zhu, Y. Xu, B.Z. Tang, M. Wang, Y. Li, Y. Zhang, M. Zhang, AIE-powered nanosoldiers for precision disruption of biofilm's extracellular defense in infection treatment, Adv. Funct. Mater. 36 (2026) e10949.
[5] Q. Ding, M. Qi, W. Li, M. Li, J. Xu, Y. Kim, G. Kim, B. Dong, L. Wang, J.S. Kim, Precision phototherapy enabled by decoding complex microenvironments, Acc. Chem. Res. 58 (20) (2025) 3167–3183.
[6] A. Bigham, M. Serrano-Ruiz, M. Caporali, I. Fasolino, M. Peruzzini, L. Ambrosio, M. G. Raucci, Black phosphorus-based nanoplatforms for cancer therapy: chemistry, design, biological and therapeutic behaviors, Chem. Soc. Rev. 54 (2) (2025) 827–897.
[7] P.H. Tong, J.J. Yang, Y.F. Zhou, Y.F. Tang, M.T. Tang, Y. Zang, Y.F. Pan, L. W. Dong, Y.X. Tan, K.T. Nam, X.L. Hu, H. Huang, J. Li, H.Y. Wang, T.D. James, J. Yoon, X.P. He, Metal-organic frameworks (MOFs) for phototherapy and synergistic phototherapy of cancer, Coord. Chem. Rev. 526 (2025) 216381.
[8] P. Chowdhury, A. Roy, S. Ghosh, Molybdenum disulfide nanomaterials for generating or depleting reactive oxygen species: recent development and prospects in biomedical applications, Small 21 (38) (2025) e06450.
[9] D. Yan, D. Wang, B.Z. Tang, Clinical and translational aspects of aggregation-induced emission, Nat. Rev. Bioeng. 3 (11) (2025) 976–991.
[10] T. Xiong, F. Ning, Y. Chen, M. Gu, M. Li, X. Chen, L. Wang, J. Fan, X. Peng, Charge regulation-enhanced Type I photosensitizer-loaded hydrogel dressing for hypoxic bacterial inhibition and biofilm elimination, ACS Nano 19 (2) (2025) 2822–2833.
[11] W. Zhou, X. Jiang, X. Zhen, Development of organic photosensitizers for antimicrobial photodynamic therapy, Biomater. Sci. 11 (15) (2023) 5108–5128.
[12] S. Yousefiasl, M. Ghovvati, M. Mirshafiei, F. Hakimi, A. Azadi, S.M.I. Moezzi, M. Yuan, F. Sefat, I. Zare, A. Maleki, Nanostructure-reinforced multifunctional hydrogels for synergistic cancer therapy, Coord. Chem. Rev. 522 (2025) 216207.
[13] B.E. Kirkpatrick, A.P. Dhand, L.P. Hibbard, M.W. Jaeschke, T. Yendamuri, B. R. Nelson, J.S. Lee, K. Bera, H.M. Zlotnick, C.A. Fox, Ultrafast-relaxing and photopolymerizable PEG hydrogels enable viscoelasticity-mediated cell remodeling in synthetic matrices, Matter 9 (2025) 102524.
[14] M. Yang, L. Chu, Y. Zhuang, C. Qi, S. Meng, Z. Liu, T. Kong, Multi-material digital light processing (DLP) bioprinting of heterogeneous hydrogel constructs with perfusable networks, Adv. Funct. Mater. 34 (32) (2024) 2316456.
[15] A. Banerjee, K. Dalsania, J. Damian, J. Asuncion, A. Masoumi, I. Noshadi, 3D digital light processing bioprinting and in situ differentiation of hiPSCs for engineering cardiac tissue, Acta Biomater. 212 (2026) 341–356.
[16] H. Chen, L. Wei, Q. Yu, C. Wang, H. Fan, M. Li, R. Dong, Y. Ma, J. Jiang, L. Deng, Injectable hydrogels for osteomyelitis treatment induce metabolic reprogramming for protection against reinfection, Nat. Commun. 17 (2026) 1613.
[17] K. Su, Y. Yan, J. Huang, Y. Chen, X. Shang, X. Wang, Y. Liu, Z. Lai, F. Song, Z. Zhang, Mitochondrial-targeted injectable hydrogel for periodontitis therapy via oral immunity and flora regulation, Bioact. Mater. 58 (2026) 348–369.
[18] K. Sakthiabirami, Y. Park, S.K. Jo, M.H. Kim, J.H. Song, Decellularized extracellular matrix (dECM) in tendon regeneration: a comprehensive review, Adv. Healthc. Mater. 15 (2026) e03676.
[19] E. Sartip, T. Behzad, M. Kharaziha, Fabrication and characterization of 3D printed agarose/poly (ethylene glycol) diacrylate/hydroxyapatite nanocomposite hydrogel for cartilage tissue engineering, Int. J. Biol. Macromol. 320 (2025) 145573.
[20] D. Palai, H. Yasue, M. Ohta, K. Uto, T. Taguchi, A. Nishiguchi, Oriented micropore-forming bioinks for 3D bioprinting of muscle tissues, Small 22 (2026) e09439.
[21] W. Liao, Y. Shi, Z. Li, X. Yin, Advances in 3D printing combined with tissue engineering for nerve regeneration and repair, J. Nanobiotechnol. 23 (1) (2025) 5.
[22] J. Wang, Y. Wang, R. Wang, Q. Wang, M. Wen, J. Wang, L. Sheng, Y. Zheng, T. Xi, A review on 3D printing processes in pharmaceutical engineering and tissue engineering: applications, trends and challenges, Adv. Mater. Technol. 10 (2) (2025) 2400620.
[23] C. Delavier, S. Bechtold, M.H. Dodds, E. Blasco, S. Ludwigs, 3D digital light processing of redox-active polymers for electrochemical applications, Adv. Funct. Mater. 36 (17) (2026) e18546.
[24] T.O. Machado, C.J. Stubbs, V. Chiaradia, M.A. Alraddadi, A. Brandolese, J. C. Worch, A.P. Dove, A renewably sourced, circular photopolymer resin for additive manufacturing, Nature 629 (8014) (2024) 1069–1074.
[25] I. Roppolo, M. Caprioli, C.F. Pirri, S. Magdassi, 3D printing of self-healing materials, Adv. Mater. 36 (9) (2024) 2305537.

[26] V. Anand, B. Bansal, M. Tyagi, A.K. Gourishetty, Engineering advanced radiation-hard plastic scintillators fabricated via DLP-based 3D-printing for radiation detection, Adv. Opt. Mater. 14 (2026) e02132.
[27] Y. Zhang, R. Davis Jr., S. Biswas, S.E. Miller, S. Raza Ur Rehman, G.T. Felix, A. K. Gaharwar, Multiscale engineered heterogeneous hydrogel composites for digital light processing 3D printing, ACS Appl. Mater. Interfaces 17 (37) (2025) 51605–51619.
[28] S. Villata, M. Canta, D. Baruffaldi, I. Roppolo, C.F. Pirri, F. Frascella, 3D bioprinted GelMA platform for the production of lung tumor spheroids, Bioprinting 36 (2023) e00310.
[29] W. Dai, L. Zhang, Y. Yu, W. Yan, F. Zhao, Y. Fan, C. Cao, Q. Cai, X. Hu, Y. Ao, 3D bioprinting of heterogeneous constructs providing tissue-specific microenvironment based on host-guest modulated dynamic hydrogel bioink for osteochondral regeneration, Adv. Funct. Mater. 32 (23) (2022) 2200710.
[30] H. Zhang, X. Sun, J. Wang, Y. Zhang, M. Dong, T. Bu, L. Li, Y. Liu, L. Wang, Multifunctional injectable hydrogel dressings for effectively accelerating wound healing: enhancing biomineralization strategy, Adv. Funct. Mater. 31 (23) (2021) 2100093.
[31] D.L. Han, Y.J. Han, J. Li, X.M. Liu, K.W.K. Yeung, Y.F. Zheng, Z.D. Cui, X.J. Yang, Y.Q. Liang, Z.Y. Li, S.L. Zhu, X.B. Yuan, X.B. Feng, C. Yang, S.L. Wu, Enhanced photocatalytic activity and photothermal effects of Cu-doped metal-organic frameworks for rapid treatment of bacteria-infected wounds, Appl. Catal. Environ. 261 (2020) 118248.
[32] Y. Wang, F. Frascella, C.G. Gaglio, C.F. Pirri, Q. Wei, I. Roppolo, Vat photopolymerization 3D printing of hydrogels embedding metal-organic frameworks for photodynamic antimicrobial therapy, ACS Appl. Mater. Interfaces 16 (42) (2024) 57778–57791.
[33] S. Wang, Z. Wang, L. Zhang, Z. Song, H. Liu, X. Xu, Sweat-adaptive adhesive hydrogel electronics enabled by dynamic hydrogen bond networks, Chem. Eng. J. 492 (2024) 152290.
[34] S. Huang, Z. Wang, Q. Wu, B. Wu, B. Chen, Y. Li, Z. Qiu, Z. Zhao, B.Z. Tang, Top-down assembly of photosensitizable flexible wood dressing with synergistic effect of anti-infection and moisture management, Adv. Funct. Mater. 35 (2025) 2423123.
[35] Y. Wang, X.L. Nie, Z.H. Lv, Y. Hao, Q.Q. Wang, Q.F. Wei, A fast hemostatic and enhanced photodynamic 2-dimensional metal-organic framework loaded aerogel patch for wound management, J. Colloid Interface Sci. 656 (2024) 376–388.
[36] J. Tan, Y. Fang, K. Wang, M. Wei, Z. Zhang, L. Wang, S. Chen, J. Pan, Carbon nanotube reinforced carbonized cellulose aerogels for enhanced hemostasis and accelerated skin wound healing, Adv. Funct. Mater. 35 (2025) 2417798.
[37] X. Jia, C. Hua, F. Yang, X. Li, P. Zhao, F. Zhou, Y. Lu, H. Liang, M. Xing, G. Lyu, Hydrophobic aerogel-modified hemostatic gauze with thermal management performance, Bioact. Mater. 26 (2023) 142–158.
[38] Y. Hou, C. Chen, K. Liu, Y. Tu, L. Zhang, Y. Li, Preparation of PVA hydrogel with high-transparence and investigations of its transparent mechanism, RSC Adv. 5 (31) (2015) 24023–24030.
[39] T. Zhang, Y. Yuan, J. Chai, X. Wu, R.K. Saini, J. Liu, X. Shang, How does dextran sulfate promote the egg white protein to form transparent hydrogel? The gelation mechanism and molecular force changes, Food Hydrocoll. 133 (2022) 107901.
[40] Y. Chen, G. Wang, P. Wang, J. Liu, H. Shi, J. Zhao, X. Zeng, Y. Luo, Metal-chelatable porphyrinic frameworks for single-cell multiplexing with mass cytometry, Angew. Chem. Int. Ed. 134 (38) (2022) e202208640.
[41] A. Cosola, I. Roppolo, F. Frascella, L. Napione, G. Barrera, P. Tiberto, F. Turbant, V. Arluison, I. Caldelari, N. Mercier, 4D printing of multifunctional devices induced by synergistic role of magnetite and silver nanoparticles in polymeric nanocomposites, Adv. Funct. Mater. 34 (41) (2024) 2406226.
[42] M. Caprioli, I. Roppolo, A. Chiappone, L. Larush, C.F. Pirri, S. Magdassi, 3D-printed self-healing hydrogels via digital light processing, Nat. Commun. 12 (1) (2021) 2462.
[43] N. Li, Z. Xiang, Y. Rong, L. Zhu, X. Huang, 3D printing tannic acid-based gels via digital light processing, Macromol. Biosci. 22 (4) (2022) 2100455.
[44] G. Mogli, M. Reina, A. Chiappone, A. Lamberti, C.F. Pirri, I. Roppolo, S. Stassi, Self-powered integrated tactile sensing system based on ultrastretchable, self-healing and 3D printable ionic conductive hydrogel, Adv. Funct. Mater. 34 (7) (2024) 2307133.
[45] C. Yao, Y. Zhao, Y. Wu, H. Wang, H. Li, J. He, L. Liu, Y. Huang, F. Cheng, Single-doped $W_{18}O_{49-x}$@au-embedded dual-network silk fibroin hydrogel for NIR-responsive phototherapeutic wound healing, Adv. Healthc. Mater. 15 (7) (2026) e03108.
[46] F. Cheng, X. Zhang, J. Dai, L. Wang, Q. Wu, L.K. Ang, H. Li, Digital light processing-printed nanozyme-integrated hydrogels enable spatiotemporal immunomodulation and repair of infected wounds, Acta Biomater. 214 (2026) 254–270.
[47] X.C. He, X.N. Chen, Y.H. Liu, X. Zhong, L. Qiang, H.Q. Wang, F.Z. Wang, J.S. Wang, C.H. Li, P.F. Zheng, A blue light 3D printable hydrogel with water absorption, antibacterial, and hemostatic properties for skin wound healing, Chem. Eng. J. 493 (2024) 152439.
[48] G.Y. Wen, X.L. Zhou, X.Y. Tian, R. Xie, X.J. Ju, Z. Liu, Y. Faraj, W. Wang, L.Y. Chu, Smart hydrogels with wide visible color tunability, NPG Asia Mater. 14 (1) (2022) 29.
[49] W. Lu, M. Rahimnejad, B.O. Sahadi, M.C. Bottino, Dopamine-conjugated methacrylated gelatin hydrogel—physical, mechanical, and biological properties, Gels 11 (2025) 499, https://doi.org/10.3390/gels11070499.
[50] W. Liao, H.B. Zhao, Z. Liu, S. Xu, Y.Z. Wang, On controlling aerogel microstructure by freeze casting, Compos. Part B Eng. 173 (2019) 107036.
[51] Q. Meng, R. Fu, L. Huang, Z. Xie, Y. Tang, K. Zhao, Resorcinol-formaldehyde resin as co-catalyst in Fenton-like reaction: synergistic enhancement of Fe^{3+}/Fe^{2+} cycling via phenolic hydroxyl redox and conjugated-structure mediated electron transfer, J. Clean. Prod. 530 (2025) 146831.
[52] Z. Liu, B. Tang, X. Gu, H. Liu, L. Feng, Selective structure transformation for NiFe/$NiFe_2O_4$ embedded porous nitrogen-doped carbon nanosphere with improved oxygen evolution reaction activity, Chem. Eng. J. 395 (2020) 125170.
[53] L. Shi, L. Yang, H. Zhang, K. Chang, G. Zhao, T. Kako, J. Ye, Implantation of iron (III) in porphyrinic metal organic frameworks for highly improved photocatalytic performance, Appl. Catal. B Environ. 224 (2018) 60–68.
[54] Z. Gong, Y. Gao, J. Li, Z. Cai, N. Liu, J. Jiang, Porphyrin-based vinylene-linked 3D covalent organic framework with unprecedented cya topology for photocatalytic H_2O_2 production, Angew. Chem. Int. Ed. 137 (13) (2025) e202423205.
[55] Y. Li, P. Sun, L. Zhao, X. Yan, D.K.P. Ng, P.C. Lo, Ferric ion driven assembly of catalase-like supramolecular photosensitizing nanozymes for combating hypoxic tumors, Angew. Chem. Int. Ed. 59 (51) (2020) 23228–23238.
[56] S. Hussain, X. Peng, L. Wang, Porphyrinic metal-organic frameworks as separation membranes: from synthesis to advanced applications, Mater. Horiz. 12 (13) (2025) 4608–4638.
[57] S. Gao, J. Liu, T. Wu, S. Li, Y. Zhang, Fe-chelated polydopamine nanoparticles prepared through photo-Fenton reaction for combined photothermal/chemodynamic antibacterial therapy, Nano Lett. 25 (29) (2025) 11291–11298.
[58] O. Hu, M. Lu, M. Cai, J. Liu, X. Qiu, C.F. Guo, C.Y. Zhang, Y. Qian, Mussel-bioinspired lignin adhesive for wearable bioelectrodes, Adv. Mater. 36 (38) (2024) 2407129.
[59] X. Zhang, F. Li, S. Liang, Y. Bai, Sweat-enhanced adhesive hydrogel enables interfacial exchange coupling for wearable strain sensor, Chem. Eng. J. 495 (2024) 153385.
[60] K. Lei, M. Chen, P. Guo, J. Fang, J. Zhang, X. Liu, W. Wang, Y. Li, Z. Hu, Y. Ma, Environmentally adaptive polymer hydrogels: maintaining wet-soft features in extreme conditions, Adv. Funct. Mater. 33 (41) (2023) 2303511.
[61] D. Chen, H. Bai, H. Zhu, S. Zhang, W. Wang, W. Dong, Anti-freezing, tough, and stretchable ionic conductive hydrogel with multi-crosslinked double-network for a flexible strain sensor, Chem. Eng. J. 480 (2024) 148192.
[62] J. Chen, W. Huang, D. Zheng, Z. Xie, X. Zhuang, D. Zhao, Y. Chen, N. Su, H. Chen, R.M. Pankow, Highly stretchable organic electrochemical transistors with strain-resistant performance, Nat. Mater. 21 (5) (2022) 564–571.
[63] Y. Zou, H.X. Liu, L. Cai, Y.H. Li, J.S. Hu, C. Liu, T.F. Liu, Strategy to efficient photodynamic therapy for antibacterium: donor-acceptor structure in hydrogen-bonded organic framework, Adv. Mater. 36 (2024) 2406026.
[64] Y. Lian, D. Lan, X. Jiang, L. Wang, S. Yan, Q. Dong, Y. Jiang, J. Gu, Z. Gao, G. Wu, Multifunctional electromagnetic wave absorbing carbon fiber/$Ti_3C_2T_X$ MXene fabric with superior near-infrared laser dependent photothermal antibacterial behaviors, J. Colloid Interface Sci. 676 (2024) 217–226.
[65] J. Zhu, H. Cheng, Z. Zhang, K. Chen, Q. Zhang, C. Zhang, W. Gao, Y. Zheng, Antibacterial hydrogels for wound dressing applications: current status, progress, challenges, and trends, Gels 10 (8) (2024) 495.
[66] Z. Hadi, A.H. Navarchian, M. Rafienia, Synthesis of pH-responsive carboxymethyl chitosan for encapsulating tetracycline-HCl: morphology, drug release behavior and antibacterial activity of microcapsules, J. Drug Deliv. Sci. Technol. 84 (2023) 104462.
[67] D. Zhang, H. Chen, Y. Zhang, J. Yang, Q. Chen, J. Wu, Y. Liu, C. Zhao, Y. Tang, J. Zheng, Antifreezing hydrogels: from mechanisms and strategies to applications, Chem. Soc. Rev. 54 (11) (2025) 5292–5341.
[68] M. Shan, X. Chen, X. Zhang, S. Zhang, L. Zhang, J. Chen, X. Wang, X. Liu, Injectable conductive hydrogel with self-healing, motion monitoring, and bacteria theranostics for bioelectronic wound dressing, Adv. Healthc. Mater. 13 (11) (2024) 2303876.
[69] D. Ningrum, W. Hanif, D. Mardhian, L. Asri, In vitro biocompatibility of hydrogel polyvinyl alcohol/*Moringa oleifera* leaf extract/graphene oxide for wound dressing, Polymers 15 (2023) 468.
[70] P. Martin, C. Pardo-Pastor, R.G. Jenkins, J. Rosenblatt, Imperfect wound healing sets the stage for chronic diseases, Science 386 (6726) (2024) eadp2974.